8-15-2017 12:00 AM

Modelling of Convective Heat Transfer in Porous Media

Jeremy Vu, *The University of Western Ontario*

Supervisor: Prof. Anthony Straatman, *The University of Western Ontario*

A thesis submitted in partial fulfillment of the requirements for the Master of Engineering Science degree in Mechanical and Materials Engineering

Abstract

This thesis details the process taken for the computational modelling of convective heat transfer in porous media with the objective of improving the accuracy of porous continuum models. CFD simulations were performed to predict convective heat transfer resulting from forced flow through highly conductive porous blocks. For the pore-level predictions, an idealized geometric model for spherical-void-phase porous materials was used to generate several domains over a range of porosity and pore diameter typical of graphitic foams. Simulation on these domains was conducted using the commercial software ANSYS CFX. Similar simulations were conducted using an in-house conjugate domain solver wherein porous regions are modelled using a porous continuum approach. These results were compared to the pore-level results and indicate that a modification to the conductivity of the solid phase of the porous material must be included to account for the tortuosity, or complexity of the solid structure. The tortuosity is shown to appear naturally in the derivation of the volume-averaged energy equation for the solid-phase constituent, and has not previously been considered when calculating the effective solid phase conductivity. The implementation of this modification resulted in a closer match of the heat transfer predicted by the in-house porous continuum model when compared to results generated by commercial CFD software. Subsequent simulations were performed to show that the tortuosity was purely a geometric function – depending only on the solid phase structure.

Acknowledgments

I thank my family for their unending love and encouragement.

I would also like to thank my supervisor Prof. Anthony Straatman for his continuous guidance, support, and patience.

To my colleagues in the Computational Fluid Dynamics Lab, I have greatly enjoyed the last two years working alongside you.

Table of Contents

Abstract i

Acknowledgments ii

List of Tables vi

List of Figures vii

Nomenclature x

Chapter 1 1

1 Background 1

1.1 Literature review 3

1.1.1 Closure parameters 4

1.1.2 Experimental studies 5

1.1.3 Geometry generation 6

1.1.4 Computational studies 11

1.2 Objectives/motivation 13

Chapter 2 15

2 Volume averaging 15

2.1 Introduction 15

2.2 Mass and momentum equations 17

2.3 Energy equation 18

2.1 Summary 21

Chapter 3 22

3 Preliminary simulations 22

3.1 Introduction 22

3.2 Geometry 22

3.3 Computational set up 24

3.4 Grid independence 27

3.5 Results 28
3.5.1 Momentum results 29
3.5.2 Thermal results 32
3.5.3 Implementation of parameters into porous continuum model 37
3.6 Summary 40
Chapter 4 41
4 Conjugate simulations 41
4.1 Introduction 41
4.2 Geometry 41
4.3 Computational set up of pore-level model 42
4.4 Grid independence 43
4.5 Computational setup of volume averaged model 44
4.5.1 Grid independence in continuum model simulations 45
4.6 Results 46
4.6.1 Momentum results 46
4.6.2 Energy results 46
4.7 Full conjugate simulation with attached substrate 50
4.7.1 Results 51
4.8 Modification of conduction within solid matrix 53
4.9 Calculating tortuosity 54
4.10 Implementation of tortuosity factor 58
4.11 Summary 63
Chapter 5 64
5 Summary and Future Work 64
5.1 Research conclusions and contributions 65
5.2 Future work 65

6 References 67

Curriculum Vitae 72

List of Tables

Table 3.1: Fluid properties of air and water used in pore-level simulations..... 24

Table 3.2: Summary of boundary conditions for isothermal simulation shown in Fig. 3.2 ... 26

Table 3.3: Summary of measured quantities showing improved accuracy as a result of increasingly fine mesh used in isothermal simulations..... 27

Table 3.4: Summary of computed parameters 28

Table 3.5: C_f and K at different geometries 32

Table 3.6: Comparison of heat transfer in isothermal case between pore-level simulations and porous continuum simulations 38

Table 4.1: Summary of boundary conditions for conjugate simulation shown in Fig. 4.1..... 43

Table 4.2: Summary of measured quantities showing improved accuracy as a result of increasingly fine mesh used in conjugate simulations 44

Table 4.3: Comparison of total heat transfer between pore level and porous continuum model using simplified geometry..... 54

Table 4.4: Summary of computed tortuosity factor for different geometries 58

List of Figures

Figure 1.1: Photographs of (a) Scanning Electron Microscope (SEM) image showing the cross section of carbon foam, and (b) an aluminum foam consisting of interconnected ligaments (taken from [1]) 1

Figure 1.2: CAD model of unit cube model geometry used for CFD simulations of porous materials. 7

Figure 1.3: Image showing modelled and actual Kelvin cell [32] used to calculate hydraulic and thermal properties 8

Figure 1.4: CAD model of modified unit cell developed by Leong and Li [34] 8

Figure 1.5: CAD model of random sphere carbon foam developed by Kirca et al. [35] 9

Figure 1.6: CAD model of periodic cubic REV developed by Chueh et al. [37] 10

Figure 1.7: CAD model of fully periodic REV developed by Dyck [38] 11

Figure 2.1: Image showing fluid and solid volume fractions within an REV (image taken from [48]) 15

Figure 3.1: Surfaces (highlighted green) where Inlet and Outlet boundary conditions were applied. This resulted in backflow, and so was not used in subsequent simulations. 23

Figure 3.2: CAD model of geometry used for preliminary isothermal simulations 24

Figure 3.3: Mesh used for preliminary isothermal simulations (Porosity 0.85 is shown) 28

Figure 3.4: Inlet and outlet surfaces of porous block 29

Figure 3.5: Pressure drop across porous block as a function of inlet velocity. 30

Figure 3.6: Velocity vector contours at Re 5, Porosity 0.75, Water, isothermal case, from y = 0 plane 31

Figure 3.7: Temperature contours at Re 5, Porosity 0.75, Water, isothermal case, from y = 0 plane 33

Figure 3.8: Outlet surface of computational domain over which bulk outlet temperature is found (note that the outlet is entirely a pure fluid region). 34

Figure 3.9: Interstitial heat transfer coefficient computed for porosity 0.75 using water as the working fluid. 36

Figure 3.10: Images showing difference between unit cube model and current geometric model produced by YADE 37

Figure 3.11: Axial pressure drop for porosity 0.75, water, Re 10, isothermal case 39

Figure 3.12: Axial bulk temperature for porosity 0.75, water, Re 10 40

Figure 4.1: CAD model of geometry used for conjugate simulations. Top shows solid and fluid geometry before mating. Bottom shows final geometry. 42

Figure 4.2: Mesh used in conjugate simulations (Porosity 0.85 is shown) 44

Figure 4.3: Mesh used in continuum model simulations 45

Figure 4.4: Velocity vector contours obtained from conjugate simulation at Re 5, Porosity 0.75, 400-micron diameter, and using water 46

Figure 4.5: Temperature contours obtained from conjugate simulation at Re 5, Porosity 0.75, 400-micron diameter, and using water 47

Figure 4.6: Plot showing comparisons of total heat transfer between pore – level simulation and porous continuum model. 48

Figure 4.7: Temperature contours obtained from porous continuum model at Re 80, Porosity 0.75, 400-micron diameter, and using water 49

Figure 4.8: Temperature contours obtained from conjugate simulation at Re 80, Porosity 0.75, 400-micron diameter, and using water 49

Figure 4.9: CAD model of geometry used for full conjugate simulations with substrate 51

Figure 4.10: Comparison of temperature contours obtained from full conjugate simulation (top) and bottom heated conjugate simulation (bottom) at Re 20, Porosity 0.85, 400-micron diameter, and using water. 52

Figure 4.11: CAD model of simplified geometry used for conjugate simulation. The geometric properties (A_{sf} and porosity) were preserved from previous porous geometries. .. 53

Figure 4.12: Streamlines of flow around cylinders emphasizing tortuosity [55] 55

Figure 4.13: Cut section of solid phase structure showing conduction paths. This is analogous to the streamlines shown in Figure 4.12; instead of flow however, heat transfer is represented by the black lines. 56

Figure 4.14: Plot showing effects of varying solid phase conductivity on total heat transfer at porosity 0.85, 400 micron diameter and using water. 59

Figure 4.15: Plot showing comparison of total heat transfer calculated using pore level CFD simulations and the porous continuum model (after implementing the tortuosity factor) at different porosities. 60

Figure 4.16: Image showing locations of lines along which average temperature is calculated 61

Figure 4.17: Plot showing comparisons between average fluid temperatures along Z axis computed by pore-level simulation and porous continuum model. 62

Figure 4.18: Plot showing comparisons between average solid temperatures along Z axis computed by pore-level simulation and porous continuum model. 62

Nomenclature

A	area, m^2
A_{sf}	denotes surface of intersection between V_f and V_s
C_f	Forcheimer coeffiecient for porous medium
$C_{p,f}$	constant pressure specific heat capacity, J/kg ·K
$C_{p,s}$	specific heat capacity for a solid, J/kg ·K
d	pore diameter, m
h	heat transfer coefficient, $W/m^2 \cdot K$
h_{sf}	Interstitial heat transfer coefficient, W/m2·K
I	identity matrix
k_f	fluid thermal conductivity, W/m·K
k_s	solid thermal conductivity, W/m·K
k_{se}	effective conductivity of solid phase, W/m·K
k_{fe}	effective conductivity of fluid phase, W/m·K
k_{disp}	dispersion conductivity
l	length scale of averaging volume (Chapter 2), m
L	length scale of porous medium (Chapter 2), m
$\dot{m}$	mass flux, kg/s
$\hat{n}$	unit-normal vector
n_{fs}	unit-normal vector directed from the fluid to solid phase on A_{fs}
Nu	average Nusselt number
p	pressure, Pa
Pr	Prandtl number
Q	overall heat transfer, W
Re_d	Reynolds number based on pore diameter d

t	time, s
T	temperature, K
T_w	wall temperature, K
T_i	inlet temperature, K
T_o	outlet temperature, K
u	fluid velocity vector, m/s
U	characteristic velocity, m/s
V	volume, m^3
$< >$	denotes extrinsic volume-average
$< >^k$	denotes intrinsic volume-average with respect to constituent k

Greek Characters:

Δ	denotes a difference
ε	porosity ($=V_f/V$)
μ, μ_f	dynamic viscosity, kg/m·s
ρ	density, kg/m
ϕ	generic scalar quantity
τ	tortuosity

Subscripts:

s	solid
f	fluid
i	inlet
o	outlet
conv	convective
LM	log mean

Chapter 1

1 Background

Porous materials have applications throughout a wide variety of engineering and science disciplines. Some examples include catalytic converters and packed bed reactors, as well as flow through soil. A porous material is essentially a two-phase structure – a solid phase, and a fluid phase. A wide range of materials fall under this definition. This can include anything from sponges, wood, or even bodily tissues.

It consists of a solid microstructure, and a working fluid. Porous materials have seen increasing use in heat transfer applications due to the high surface area-to-volume ratio. This is the same reason fins are used in cooling applications as heat sinks, however the surface area of porous materials is often much greater. In this application, a cooling fluid is forced through the porous material (or fins), and draws heat away from the surface. Figure 1.1 shows close-up images of typical porous materials.

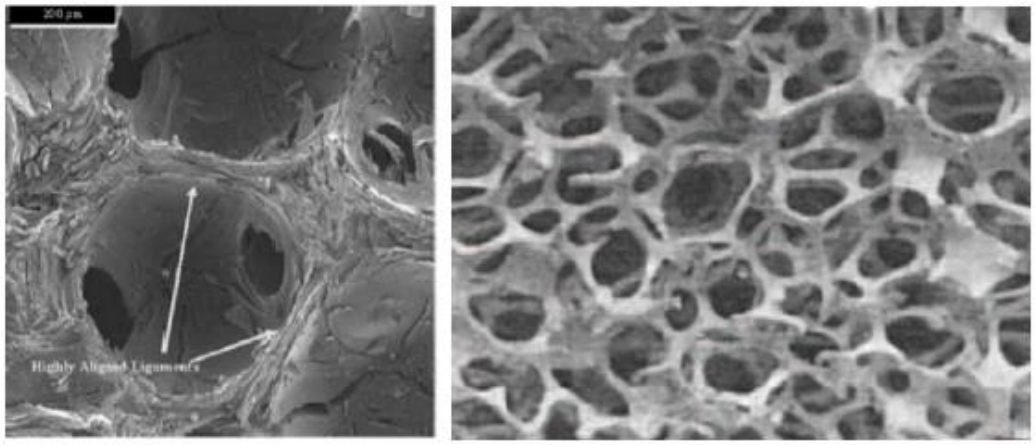

Figure 1.1: Photographs of (a) Scanning Electron Microscope (SEM) image showing the cross section of carbon foam, and (b) an aluminum foam consisting of interconnected ligaments (taken from [1])

There are many different shapes or structures when using porous materials. One such is reticulated structures, shown in Fig. 1.1(b). Other examples include spherical – void phase, in which graphite is a commonly used material. This was developed by Oak Ridge National Laboratory, and have a much higher effective thermal conductivity than aluminum foams. This is due to two reasons: the material conductivity of graphite is higher than that of aluminum's, and the spherical void phase structure results in a much higher surface area to volume ration when compared to the reticulated structure. The combination of these attributes make such materials an excellent choice for enhanced heat transfer applications such as heat sinks or heat exchangers. Straatman et al. [2,3,4,5,6] performed experiments using flow configurations such as parallel, impinging, and internal flow to evaluate the performance of graphite foams, which had the spherical void-phase structure. It was found that enhancements in heat transfer were significant when compared with aluminum foams, however the pressure drop is higher than that found when using aluminum or reticulated foams.

Due to their applications in convective heat transfer, it follows that porous materials must be properly characterized so that engineers may design with them using the same principles as heat sinks. Before the design process, however, they must be modelled to predict performance. This can be done using pore level simulations. Pore level means that the full instantaneous Navier Stokes equations are solved for the entire flow and temperature field inside the porous structure. This presents some drawbacks – first is that it is very computationally expensive due to the complicated geometry of porous materials. Second, until recently there was no way to generate physically accurate porous geometry for CFD.

To circumvent these issues, the Navier Stokes equations can be volume averaged. This process treats the porous medium as a continuum comprised of the solid and fluid phases. The mass and momentum equations treat the porous medium as a single continuum. The energy equation is slightly different. When local thermal non-equilibrium (LTNE) is assumed, the fluid and solid phase energy equations are treated separately – a separate energy equation is used for each. LTNE implies that there is a temperature difference between the two phases of the porous material. On the other hand, when assuming local

thermal equilibrium (meaning there is no temperature difference between the fluid and solid phases), the domain is treated as a single continuum, and assigns a single temperature for both the fluid and solid phases. In enhanced heat transfer applications, the conductivity ratio between the solid and fluid phase is quite high, and thus the assumption of local thermal equilibrium is invalid.

Many codes and numerical algorithms have been developed to solve these volume-averaged equations. Among these, a structured porous continuum code was developed by Betchen [7] (which will be referred to herein as the porous continuum model) using local thermal non-equilibrium in which the porous material is treated as a continuum. Calibration was required before the model could be used to accurately predict the heat transfer and flow fields, and was validated using graphite foams [5]. Correlations exist which calculate the thermophysical properties [8], however these were only applicable to the reticulated foams mentioned previously. Calibration must be performed using experimental results, or, as in the case of this work, pore level simulations.

The methodology used in the porous continuum model gives very good results, as seen in the validation. However, despite calibration, there are still some cases where the errors grow unacceptably large – up to 50% when compared to results generated from commercial CFD software. If the model is to be used in the design process, the accuracy must be improved. This chapter will serve as an introduction and literature review in the topics of closure parameters, experimental studies, geometry generation, and computational studies of porous media. This will lay the groundwork for the material shown in the subsequent chapters.

1.1 Literature review

The following section will review the current literature as it relates to modelling transport in porous media, with specific focus on heat transfer applications and high-conductivity porous foams. It starts with an overview of the closure parameters that must be computed before solving the volume-averaged governing equations It will then move on to experiments performed on porous media, as that was the earliest method of studying such

materials. Geometry generation will then be examined. Finally, a review of computational studies will be presented.

1.1.1 Closure parameters

Porous materials have several parameters that describe them. When the governing equations are volume-averaged, closure models must be developed that relate the pore level physics to the volume-averaged level. This is because after applying the volume-averaging operator, there are still variables that remain which depend on the local transport variables. Since the purpose of the volume-averaged equations is to solve for the bulk flow and thermal fields, these pore-level variables must be resolved to provide a closed set of equations which does not rely on the spatial deviations. This is generally done either heuristically, or using constitutive relations. Closure models have been developed for both the momentum equation by Whitaker [9] and the energy equation by Quintard et al. [10], which operates under local thermal non-equilibrium. It should be noted that while there are many studies focusing on closure for thermal equilibrium [11-15], it is considered not applicable in the present work due to the large difference in conductivities between the solid phase and the working fluid and the large temperature differences that are often encountered in heat transfer applications.

In the momentum equation, the pressure drop must be related to the bulk velocity. One of the most basic models, Darcy's law, shown in Eq. (1.1), is presented in [16]:

$$-\nabla p = \frac{\mu}{K}\langle \mathbf{u} \rangle \tag{1.1}$$

In this equation, p is pressure, K is the permeability, and the average velocity vector is given by $\langle \mathbf{u} \rangle$. Unfortunately, Darcy's law is only applicable to flows at very low Reynolds number – at higher Reynolds number, the linear relationship between pressure and velocity no longer holds. Darcy's Law as it stands is, therefore, not practical for many flows encountered in engineering applications. To account for this, an additional term must be used. Ward [17] added a quadratic term which accounts for the inertial effects. The new expression is shown in Eq. (1.2). The C_E term is referred to as the

Forcheimer coefficient. At low Reynolds numbers, the quadratic term is effectively zero, and can be neglected – reducing to the Darcy's Law.

$$-\nabla p = \frac{\mu}{K}\langle \mathbf{u} \rangle + \frac{\rho C_f}{\sqrt{K}}\langle \mathbf{u} \rangle \langle \mathbf{u} \rangle \tag{1.2}$$

In the energy equation, there is convection at the interface between the solid and fluid phases of the porous material, with the heat transfer being driven by the temperature difference between the two phases. The interstitial heat transfer coefficient (denoted by the variable h_{sf}) determines the level of heat transfer. All the parameters previously discussed can be determined experimentally, or, as in later cases, numerically.

1.1.2 Experimental studies

The earliest method of studying porous geometry was through experimental means. This was before the widespread use of CFD, as well as before porous geometry could easily be modelled. To do this, a physical representation of the porous material was obtained, and experiments would be carried out. Gallego and Klett [18] performed such experiments to evaluate heat transfer coefficients. Straatman et al. [19] determined hydraulic and heat transfer coefficients for four different graphitic foams, and have developed correlations for the interstitial heat transfer coefficient. The experiment measured the temperature difference across a heated foam block, and used the following expression for the Nusselt number:

$$Nu = \frac{q}{A_{eff}\Delta T} \tag{1.3}$$

A_{eff} is the effective area, and an estimate can be calculated using correlations. Fu et al. [20] correlated the interstitial heat transfer coefficients of cellular ceramics in the form of $Nu = CRe^m$. Another study by Kamiuto and Yee [21] compiled different studies [22,23] and found that a fairly accurate correlation exists when the strut diameter is used as a characteristic length in open cell foams. Ando et al [24] experimentally determined the h_{sf} for ceramic foams. This method differs from that used by Straatman et al. – a "single blow method" was used instead. In this method, the transient temperature response is

measured. Hot air is passed through a porous block, and once steady state has been achieved, the heat supply to the air is suddenly cut off. This introduces a temperature difference, and the system becomes transient. The volume averaged energy equations (under thermal non-equilibrium) are then solved, and the h_{sf} is adjusted so that the volume averaged results match the experiments. It is emphasized that the determination of h_{sf} is extremely important, as it is the parameter which characterizes heat transfer, and accurate determinations must be made to ensure proper results.

The Forcheimer coefficient and permeability has also been of interest. Jambhekar [25] uses experimental data to fit these coefficients. Different regression methods were used, depending on the desired accuracy. From performing both isothermal and non – isothermal experiments, it was found that the local thermal equilibrium assumption is not appropriate since it fails to match the non-isothermal experimental results. Other studies include those done by Calmidi et al [26], which had experiments (as well as numerical simulations) performed on aluminum foams to study the effect of thermal dispersion. Results showed that dispersion is negligible when air is used as the working fluid, however its effects are much more significant when water is used instead.

1.1.3 Geometry generation

Pore level simulations are inherently difficult to conduct. Firstly, the geometry needed is difficult to generate. One method is to use reconstruction from Computer Tomography scans. A digital representation of the physical sample of interest is obtained and discretized, allowing simulations to be performed. Some notable examples include work done Haussener et al, in which hydraulic, thermal, and radiative transport properties were obtained for materials such as porous ceramics [27], reacting packed beds [28,29] and snow [30].

Using 3D modelling software, many geometries are simply cylinders arranged in a periodic fashion, as the periodicity plays a significant role in simplifying the computational boundary conditions. The unit cube model (shown in Fig. 1.2) was then developed [31], allowing the porosity to be prescribed, while still retaining the periodicity.

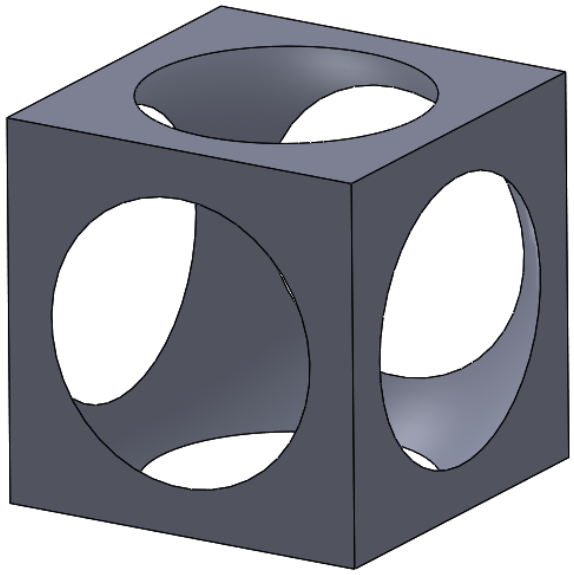

Figure 1.2: CAD model of unit cube model geometry used for CFD simulations of porous materials.

These are created by hollowing a single pore out of a cube until the desired porosity is achieved; the geometry is simple, which makes it easy to calculate parameters such as porosity and surface area. Yu et al. [31] used the unit-cube model to examine the hydraulic and thermal properties of spherical void phase porous media, but found that estimates of the permeability led to pressure drops that were unrealistically low. Boomsma & Poulikakos [32] proposed a different geometry – a tetrakaidekahedron shape (or the Kelvin cell). This Kelvin cell, shown in Fig. 1.3, was used to calculate hydraulic and thermal properties by authors Kumar et al. [33].

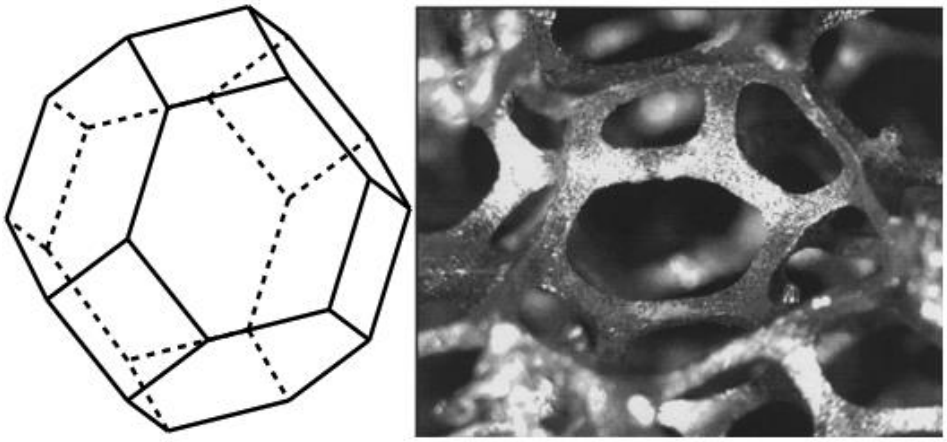

Figure 1.3: Image showing modelled and actual Kelvin cell [32] used to calculate hydraulic and thermal properties

Another addition to the unit cube family was proposed by Leong and Li [34], in which spheres are subtracted from the corners of a cube, shown in Fig. 1.4. This was used to evaluate hydrodynamic and thermal properties of carbon foam.

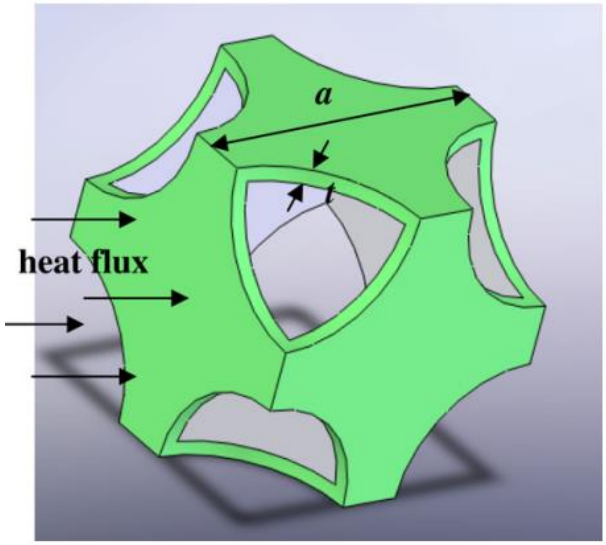

Figure 1.4: CAD model of modified unit cell developed by Leong and Li [34]

There are many drawbacks to the unit cube model however, because its simplicity. Simply put – they are not physically realistic. The pores are equally sized, and the model is isotropic. Many attempts have been made to improve this. Kirca et al. [35] placed

random bubbles inside a cube, and modified the bubble radii, average bubble radius, and neighboring bubble interactions to obtain a desired porosity. The geometry, shown in Fig. 1.5 was used to determine Young's modulus and poisons ratio, but not heat transfer coefficients.

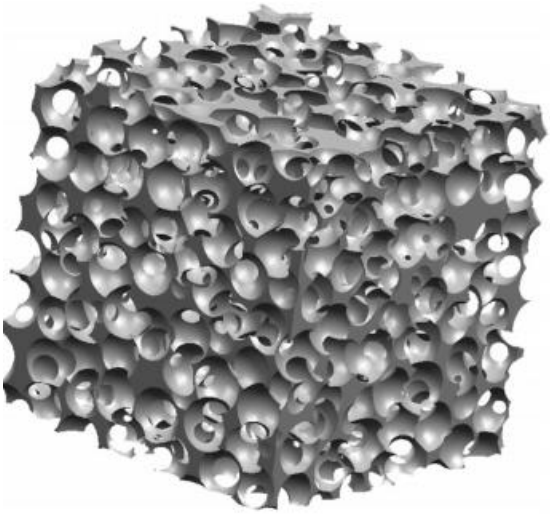

Figure 1.5: CAD model of random sphere carbon foam developed by Kirca et al. [35]

A random-generation was proposed by Wang & Pan [36], where open-cell foams are modelled by randomly generating points and then linking neighboring nodes using stochastic methods. The method was used to determine thermal conductivity. Notably, Chueh et al. [37] created cubic REVs (shown in Fig. 1.6) which were periodic in two directions. These were used, again to predict thermal conductivity.

Figure 1.6: CAD model of periodic cubic REV developed by Chueh et al. [37]

In 2012, Dyck [38] used Discrete Element Modeling (DEM) to create a fully periodic, cubic domain, shown below in Fig. 1.7. The model uses a contact law based on bubble physics which handles the interaction and interference between spheres. The sphere diameters are random within a specified interval, and the volume is compressed to obtain a desired porosity.

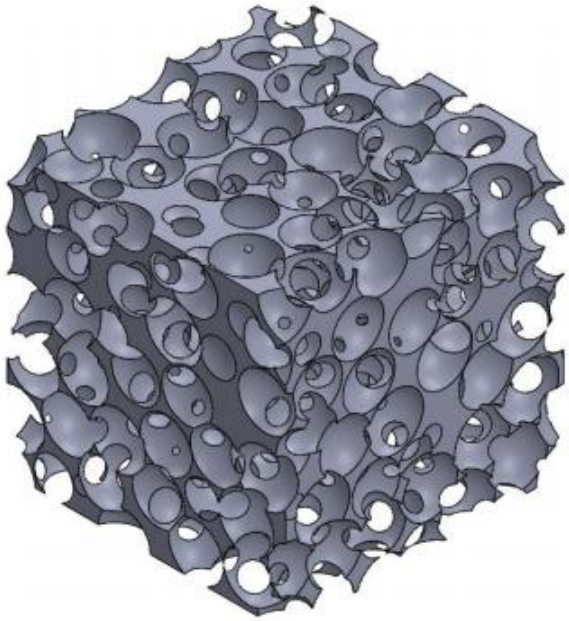

Figure 1.7: CAD model of fully periodic REV developed by Dyck [38]

This geometry was used to determine radiative transport properties in porous materials. As well, it was shown that this model was much more effective at predicting hydraulic and thermal properties than the unit cube model.

1.1.4 Computational studies

With the rise of CFD, along with the increased capabilities to reproduce geometry in CAD software, more numerical simulations are being performed to investigate the behavior and characterization of porous materials. Kopanidis et a. [39] used the Kelvin cell geometry to model conjugate heat transfe. Simulations involving both the fluid and solid phase were performed. The geometry was described with a 3D numerical model, and used a tetrahedral volume mesh for both phases. An in-house FORTRAN code was used to solve the Navier-Stokes and energy equations. Comparisons were made between the numerical results and experimental results, which showed good agreement in both flow fields and temperature fields. Unlike the present work, which will focus on spherical-void phase geometries; this study utilized a structure which was more ligament based.

Bianchi et al. [40] used a scale-resolving approach to investigate the heat transfer near the wall of sponges packed into a tubular reactor. CFD models based on X-ray computed tomography was utilized in different studies [41,42] to compute interstitial heat transfer coefficient and pressure drop values. A finite volume direct pore-level numerical simulation was used to solve for the instantaneous Navier-Stokes equations, and results were in good agreement with experimental results. Meinicke et al [43] also performed CFD modelling of heat transfer in solid sponges, using a scale – resolving technique, at a reasonable computational cost. The scale-resolved CFD calculations are applied only to representative elementary volumes within the porous material, rather than the whole porous domain. These pore level calculations are then coupled with the rest of the domain, which are modelled as a porous continuum. Bodla et al. [44] developed a 1D conduction model used to estimate the effective thermal conductivity of open-celled metal foams. An analogy between electrical and thermal conduction led to a new resistance model which could compute values for the effective thermal conductivity quickly. Karimian and Straatman [45] used direct simulations to model flow and heat transfer to gain insight into axial dispersion. Straatman et al. [46] performed the pore-level simulations using the geometry proposed by Dyck and Straatman, which resulted in a simplified 1D model for heat transfer. Air was used as the working fluid, and the 1D model was based on the temperature profile equation for an extended surface. Results indicated a reasonable match between the 1D model and that predicted by commercial CFD, however at higher Reynolds numbers the prediction is off by 10%. It was possible that the back conduction along the axial direction is the reason for these errors.

While the previous studies present good agreement between numerical results, they still require the instantaneous Navier-Stokes equations to be solved at the pore level. As a more time-efficient alternative to pore-level simulations, which are computationally expensive due to the complex geometries involved, the volume-averaged governing equations can be solved instead. Volume-averaging is used to simplify the governing equations (a more in-depth analysis will be performed in Chapter 2). Before solving the volume-averaged equations, the closure parameters and the porous material properties must be computed. Betchen et al. developed a 3D finite-volume code (the porous continuum model) that solves the volume-averaged transport equations [7] in the porous

regions of conjugate domains. The code was validated against standard problems such as the porous plug and the Beaver-Josephs problem [47] in terms of global parameters. DeGroot expanded the solver to include unstructured grids [48], and provided an in-depth analysis of the dispersion conductivity. In a work by Zhang et al [49], a comparison was made between volume-averaged and pore-scale simulations in terms of thermal radiation and natural convection. In this particular case, the volume-averaged model not only saves time, and also provided reasonable results when comparing against experimental results. Costa et al [50] employed a control-volume finite-element method to implement the stress jump condition at an interface between a porous material and a pure fluid region. The resulting implementation was tested with the Beavers Joseph problem [47] and matched well with analytical results. DeGroot et al. [51] performed a numerical study using the porous continuum model to investigate the forced convective heat transfer in heat sinks. Aluminum foam was placed between the fins of the heat sink to enhance heat transfer, and this effect was studied and compared to experimental results. It was found that the total heat transfer predicted by the model showed the correct trends, but did not entirely match the results obtained from experiments, which suggests there may still be deficiencies in the formulation of the porous continuum model.

1.2 Objectives/motivation

This thesis aims to reconcile the differences seen between the porous continuum model and the results seen in pore level CFD simulations. Pore level simulations will be conducted, and compared with results generated by the porous continuum model code written by Betchen et al. [7]. The pore level simulations will be conducted using the random geometry YADE model created by Dyck and Straatman [38]. Preliminary pore-level simulations are performed to compute the closure parameters which will then be input to the porous continuum model. The momentum equation and mass equation use a form coefficient and permeability closure model. The energy equation requires the interstitial heat transfer coefficient, and the exposed surface area.

The motivation of this thesis is to improve the accuracy of the porous continuum solver, allowing CFD simulations of the key thermofluid outcomes to be performed more efficiently. The overarching goal of this thesis will be to improve the capabilities of the

porous continuum model, and to show a validated method of calculating the proper parameters needed to characterize a porous structure.

Chapter 2

2 Volume averaging

2.1 Introduction

This chapter will focus on the process of volume-averaging the governing equations. Volume-averaging can be thought of as analogous to Reynolds averaging. Rather than directly solving the Navier-Stokes equations for a porous material, the equations are instead averaged so that only the bulk – or volume-averaged – effects are predicted. It is assumed that the working fluid is Newtonian and incompressible, and that the porous material is isotropic (from the macroscopic level). After volume-averaging, the equations still have some remaining terms that involve the pore-level deviations in velocity, pressure and temperature. Closure models will be applied at that point which replace these pore-level variables with empirical parameters.

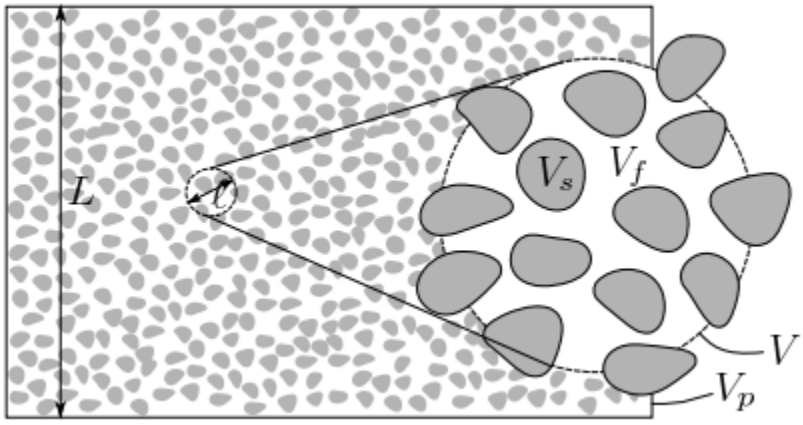

Figure 2.1: Image showing fluid and solid volume fractions within an REV (image taken from [48])

A typical representative elementary volume (REV) is shown in Fig. 2.1, where L is the length scale of the domain, l is the length scale of the representative elementary volume, V_p is the volume of the domain, and V is the averaging volume, or REV. As the name implies, the REV is the smallest volume, which is representative of the entire domain. The volume V must be large enough that the volume-average at a point is unaffected by

the choice of volume, yet small enough that the quantity (be it temperature, velocity, or pressure) is assumed constant throughout the averaging volume. In practice, this volume is usually determined through progressively selecting smaller volumes until the previous criteria is met. For a more detailed description and illustration of the process, refer to [48]. The following mathematical definitions can then be presented, where Eq. (2.1) is the extrinsic or superficial average of a scalar quantity ϕ, where m denotes the phase over which the quantity is averaged over. The intrinsic average can similarly be defined in Eq. (2.2), and the two are related through Eq. (2.3).

$$\langle \phi_m \rangle \stackrel{\text{def}}{=} \frac{1}{V} \int_{V_m} \phi_m dV \tag{2.1}$$

$$\langle \phi_m \rangle^m \stackrel{\text{def}}{=} \frac{1}{V_m} \int_{V_m} \phi_m dV \tag{2.2}$$

$$\langle \phi_m \rangle = \varepsilon \langle \phi_f \rangle^f \; if \; m = f \; ; \; (1-\varepsilon)\langle \phi_s \rangle^s \; if \; m = s \tag{2.3}$$

Another important definition to be used is the Spatial Averaging Theorem (SAT), shown in Eq. (2.4). This is used when the averaging is applied to derivatives – rather, what is needed is not the average of derivatives, but the derivative of averages.

$$\langle \nabla \phi_m \rangle = \nabla \langle \phi_m \rangle + \frac{1}{V} \int_{Amn} \hat{\mathbf{n}} \phi_{mn} dA \tag{2.4}$$

Another important expression is required when dealing with the volume-average of products of variables. This is dealt with by Whitaker as a decomposition of the variable into an intrinsic volume-average and a pore-level spatial deviation, shown in Eq. (2.5). The volume-average of a product of variables is then defined in Eq. (2.6):

$$\phi_m = \langle \phi_m \rangle^m + \check{\phi}_m \tag{2.5}$$

$$\langle \phi_{m,1} \phi_{m,2} \rangle = \frac{1}{\varepsilon_m} \langle \phi_{m,1} \rangle \langle \phi_{m,2} \rangle + \langle \tilde{\phi}_{m,1} \tilde{\phi}_{m,2} \rangle \tag{2.6}$$

It is safe to assume that the volume-average of spatial deviations is zero [3], as well as assuming that volume-averaged quantities are constant within the averaging volume, which was one of the original requirements for the selection of the averaging volume. Using the presented definitions, the volume averaging process can be carried out on the mass, momentum, and energy equations. The following derivations have been carried out in the past [38,48], and can be examined in greater detail in those works.

2.2 Mass and momentum equations

The instantaneous (or pore level) mass and momentum equations (Eq. 2.7 and Eq. 2.8), and their volume averaged counterparts (Eq. 2.9 and Eq. 2.10), are presented below.

$$\nabla \cdot \mathbf{u} = 0 \tag{2.7}$$

$$\rho_f \left(\frac{\partial \mathbf{u}}{\partial t} + \mathbf{u} \cdot \nabla \mathbf{u} \right) = -\nabla p + \mu_f \nabla^2 \mathbf{u} \tag{2.8}$$

$$\nabla \cdot \langle \mathbf{u} \rangle = 0 \tag{2.9}$$

$$\begin{aligned} \rho_f \left(\frac{\partial \langle \mathbf{u} \rangle}{\partial t} + \frac{\langle \mathbf{u} \rangle}{\varepsilon} \cdot \nabla \langle \mathbf{u} \rangle \right) & \\ = -\varepsilon \nabla \langle p \rangle^f + \mu_f \nabla^2 \langle \mathbf{u} \rangle & \\ + \frac{1}{V} \int_{A_{fs}} \left(-\tilde{p} \mathbf{n}_{fs} + \mu_f \nabla \tilde{\mathbf{u}} \cdot \mathbf{n}_{fs} \right) dA - \rho_f \nabla \cdot \langle \tilde{\mathbf{u}} \tilde{\mathbf{u}} \rangle & \end{aligned} \tag{2.10}$$

The momentum equation presents a closure problem – the pore level pressure and velocity terms are still present. The purpose of the volume – averaged equations is to solve for the bulk flow and thermal fields. As such, the pore level pressure and velocity terms must be resolved in such a way that the final set of equations no longer depends on the pore level variables. One way in which this is dealt (and which will be used in this thesis), is replacing these terms with an empirical Darcy coefficient (K) and Forcheimer constant (C_f), terms which arise from the extended Darcy equation. This is the approach used by Vafai and Tien [1]. This reduces the momentum equation to the form shown below.

$$\rho_f\left(\frac{\partial\langle\mathbf{u}\rangle}{\partial t}+\frac{\langle\mathbf{u}\rangle}{\varepsilon}\cdot\nabla\langle\mathbf{u}\rangle\right)=-\varepsilon\nabla\langle p\rangle^f+\mu_f\nabla^2\langle\mathbf{u}\rangle-\frac{\varepsilon\mu_f}{K}\langle\mathbf{u}\rangle-\frac{\varepsilon\rho_f C_f}{\sqrt{K}}|\langle\mathbf{u}\rangle|\langle\mathbf{u}\rangle \tag{2.11}$$

Here the permeability K and the Forcheimer coefficient C_f are introduced. These parameters are related to the pressure drop through the equation shown below, as developed by Ward [17].

$$-\nabla\langle p\rangle^f=\frac{\mu_f}{K}\langle\mathbf{u}\rangle-\frac{\rho_f C_f}{\sqrt{K}}|\langle\mathbf{u}\rangle|\langle\mathbf{u}\rangle \tag{2.12}$$

The momentum and mass equations have now been volume-averaged, and with the specification of K and C_f, have no specific dependency on the pore-level physics.

2.3 Energy equation

The fluid and solid phase energy equations are shown below.

$$\rho_f C_{p,f}\left(\frac{\partial T_f}{\partial t}+\mathbf{u}\cdot\nabla T_f\right)=k_f\nabla^2 T_f \tag{2.13}$$

$$\rho_s C_{p,s}\frac{\partial T_s}{\partial t}=k_s\nabla^2 T_s \tag{2.14}$$

After volume averaging, the equations become:

$$\begin{aligned}\rho_f C_{p,f}&\left(\frac{\partial\langle T_f\rangle^f}{\partial t}+\langle\mathbf{u}\rangle\cdot\nabla\langle T_f\rangle^f\right)\\&=k_f\nabla^2\langle T_f\rangle^f+\nabla\cdot\left(\frac{1}{V}\int_{A_{fs}}k_f\tilde{T}_f\mathbf{n}_{fs}dA\right)\\&\quad+\frac{1}{V}\int_{A_{sf}}k_f\nabla\tilde{T}_f\cdot\mathbf{n}_{fs}dA-\varepsilon\rho_f C_{p,f}\nabla\cdot\langle\tilde{\mathbf{u}}\tilde{T}_f\rangle^f\end{aligned} \tag{2.15}$$

$$(1-\varepsilon)\rho_s C_{p,s}\frac{\partial\langle T_s\rangle^s}{\partial t} = (1-\varepsilon)k_s\nabla^2\langle T_s\rangle^s + \nabla\cdot\left(\frac{1}{V}\int_{A_{fs}} k_s\tilde{T}_s\mathbf{n}_{fs}dA\right) + \frac{1}{V}\int_{A_{sf}} k_s\nabla\tilde{T}_s\cdot\mathbf{n}_{fs}dA \tag{2.16}$$

It should be noted that local non-thermal equilibrium is assumed – that is, there a distinct temperature for both the fluid and the solid phase, rather than one uniform average temperature. The pore level temperature deviations present must be dealt with. The last term on the RHS of the energy equation governs the heat transfer between the solid and fluid phases. This is usually modeled using Newton's Law of cooling. h_{sf} is the interstitial heat transfer coefficient, and A_{sf} is the exposed surface area over which heat transfer occurs.

$$\frac{1}{V}\int_{A_{sf}} k_f\nabla\tilde{T}_f\cdot\mathbf{n}_{fs}dA = -h_{sf}A_{sf}\left(\langle T_f\rangle^f - \langle T_s\rangle^s\right) \tag{2.17}$$

$$\frac{1}{V}\int_{A_{sf}} k_s\nabla\tilde{T}_s\cdot\mathbf{n}_{fs}dA = -h_{sf}A_{sf}\left(\langle T_s\rangle^s - \langle T_f\rangle^f\right) \tag{2.18}$$

The 2nd last term is referred to as the Tortuosity term. Quintard et al. developed a two-equation model [2], which when applied gives the following:

$$k_s\frac{1}{V}\int_{A_{fs}}\mathbf{n}_{fs}\tilde{T}_s dA = k_s\frac{1}{V}\int_{A_{sf}}\mathbf{n}_{sf}\mathbf{b_s}\cdot\nabla\langle T_s\rangle^s dA = \nabla\langle T_s\rangle^s\cdot k_s\frac{1}{V}\int_{A_{sf}}\mathbf{n}_{sf}\mathbf{b_s}dA \tag{2.19}$$

Inserting this back into the energy equation yields:

$$(1-\varepsilon)\rho_s C_{p,s}\frac{\partial\langle T_s\rangle^s}{\partial t} = \nabla\cdot\left((1-\varepsilon)k_s\mathbf{I}+k_s\frac{1}{V}\int_{A_{sf}}\mathbf{n}_{sf}\mathbf{b_s}dA\right)\cdot\nabla\langle T_s\rangle^s - h_{sf}A_{sf}\left(\langle T_s\rangle^s-\langle T_f\rangle^f\right) \tag{2.20}$$

The bracketed terms on the RHS of the equation is grouped together into a single quantity – the conductivity tensor:

$$\mathbf{K}_{se} = (1-\varepsilon)k_s\mathbf{I}+k_s\frac{1}{V}\int_{A_{sf}}\mathbf{n}_{sf}\mathbf{b_s}dA \tag{2.21}$$

Since an isotropic medium is assumed, this tensor reduces to a diagonal matrix, in which the effective thermal conductivity remains. This conductivity is of interest in this work. It consists of three parts – the conductivity of the material, the conductivity due to the effects of dispersion, and the conductivity due to the effects of tortuosity. The effective conductivity can then be written as:

$$k_{se} = \frac{k_s}{\tau}*(1-\varepsilon)+k_{disp} \tag{2.22}$$

The tortuosity τ is defined as the length of a particle path, over the distance between the two end points, and will be the focus of a subsequent chapter. As such, it will always be greater than 1. This factor, and its effects on heat transfer, will be the main focus in later chapters. The volume averaged energy equation for the solid phase is therefore:

$$(1-\varepsilon)\rho_s C_{p,s}\frac{\partial\langle T_s\rangle^s}{\partial t} = k_{se}\nabla^2\langle T_s\rangle^s - h_{sf}A_{sf}\left(\langle T_s\rangle^s-\langle T_f\rangle^f\right) \tag{2.23}$$

The fluid energy equation is closed in the exact same manner, with the addition of a convection term. Applying the theorems discussed previously, the fluid phase energy equation is finally given as:

$$\rho_f C_{p,f}\left(\frac{\partial\langle T_f\rangle^f}{\partial t}+\langle\mathbf{u}\rangle\cdot\nabla\langle T_f\rangle^f\right)=k_f\nabla^2\langle T_f\rangle^f-h_{sf}A_{sf}\left(\langle T_f\rangle^f-\langle T_s\rangle^s\right) \tag{2.24}$$

2.1 Summary

In this chapter the theory behind volume averaging is explained, and the volume averaged governing equations are presented. The pore-level variables that remain after the volume averaging process are resolved using closure models which introduce parameters relating the pore-level physics to the volume-averaged level. Local thermal non-equilibrium is assumed in the porous region, resulting in two separate energy equations for the solid and fluid constituents. After computing the values for the closure parameters, these equations will be solved using an in-house finite volume code.

Chapter 3

3 Preliminary simulations

3.1 Introduction

Recall that the volume-averaged equations require closure parameters to be solved. These parameters are: the Forcheimer coefficient (C_f), the permeability (K), and the interstitial heat transfer coefficient (h_{sf}). Rather than performing experiments to obtain these parameters, the geometry produced by the YADE model enables accurate pore level simulations to be performed from which the parameters can be evaluated. This chapter will detail the preliminary simulations – the sole purpose being to compute the closure parameters required for the volume averaged 3D code. The pore level simulations are conducted using ANSYS CFX, while the volume-averaged simulations employ an in-house, structured finite volume solver (the porous continuum model). These simulations were performed for each different geometry (blocks with different porosity). When a different fluid is used, all three parameters must be recalculated. However, when the conductivity of the porous block is changed, these parameters stay the same. This is because the heat transfer coefficient is not dependent on the heating conditions (i.e. the conductivities and temperature differences) since the Nusselt number is generally only a function of the Reynolds number and Prandtl number. Once these parameters are established, they can be input into the volume-averaged code. The simulations were run over the range of Reynolds number 1 to 200 (10 cases within this range). This was considered a large enough range in the laminar regime – beyond this the flow regime transitions to turbulence. A REV is modelled – which means that the volume is small enough such that the solid phase temperature can be set to a constant temperature, as well as a uniform mass flow rate at the inlet.

3.2 Geometry

The geometry used for the isothermal case is shown on the following page. A single porous block is used to model the REV. Previous work [38] has established this to be an accurate representation. The pore-level simulations were carried out on geometric models generated by the YADE code [38]. Geometric models were generated for a pore diameter

of 400 microns and porosities 0.75, 0.8 and 0.85. The pore diameter and porosities were chosen due to being the standard size ranges that porous materials are used for in heat transfer applications.The geometric models were converted to CAD models in SolidWorks and then imported into ANSYS Workbench and subsequently meshed using the ANSYS Meshing tool. A more detailed discussion of the grid and independence study is presented in a subsequent section.

An inlet and outlet length of 1mm was used – both to avoid having to deal with backflow in the boundary conditions. Due to the geometry being considered as a REV, the definition implies that a uniform mass flow rate across the volume is realistic and expected. It was found that if a uniform mass flow is specified directly at the inlet face of the porous block (without the 1mm lead up), the solver experiences problems with backflow at this surface, and will not converge. The same issue is experienced if an outlet condition is specified directly at the outlet surface of the porous block. Figure 3.1 shows this in picture format – the green surfaces are the inlet and outlet, and the flow is in the direction of the arrows shown. The sides not highlighted were specified as translationally periodic with their paired face.

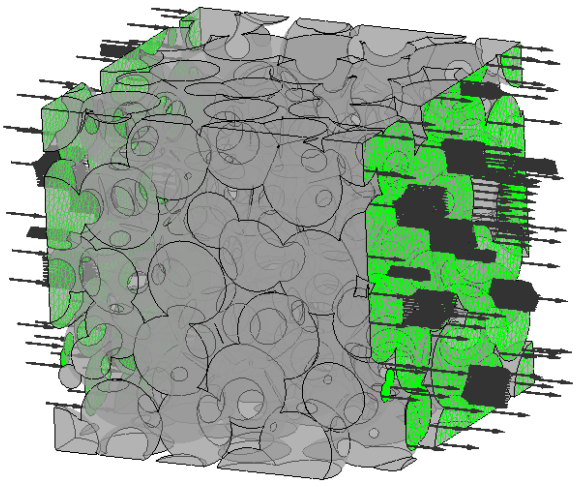

Figure 3.1: Surfaces (highlighted green) where Inlet and Outlet boundary conditions were applied. This resulted in backflow, and so was not used in subsequent simulations.

This geometry is considered an REV, as defined earlier. Because of the definition of an REV, it is reasonable to impose an isothermal condition in the solid phase, and subsequently the interior of the solid phase does not require meshing. The CAD model of the geometry used for meshing and conducting the simulations is shown in Fig. 3.2. The porous block itself is a cube, and has an edge length of roughly 1.5mm, depending on the porosity specified during the geometry generation. The inlet and outlet length is 1mm as mentioned previously. 100 spheres were used in the generation of the geometry (the sphere in spherical void-phase), as this was found in previous work to be a sufficient number of spheres needed to accurately represent porous geometry [38].

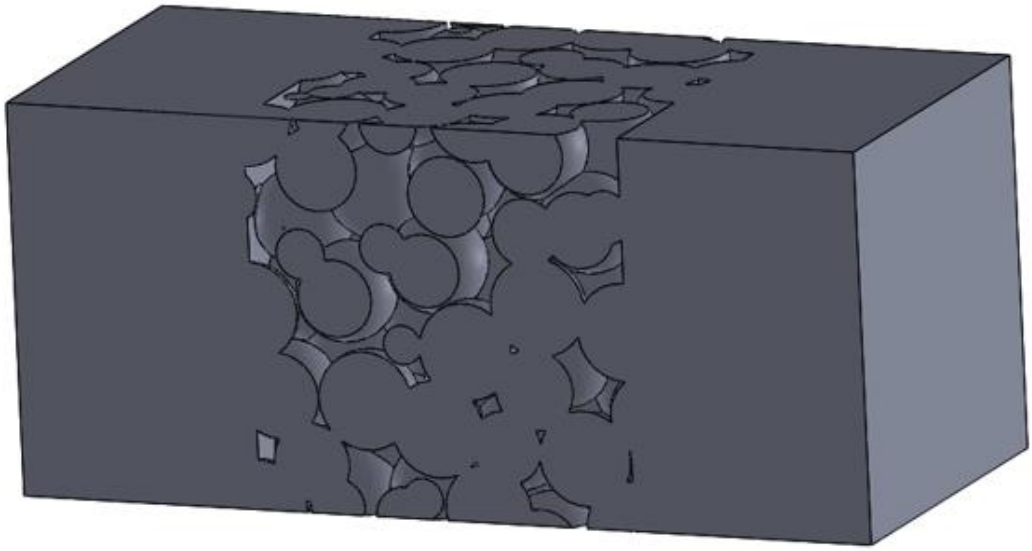

Figure 3.2: CAD model of geometry used for preliminary isothermal simulations

3.3 Computational set up

Two different working fluids were used in the simulations: air, and water. Their properties at 25ºC are shown below in Table 3.1.

Table 3.1: Fluid properties of air and water used in pore-level simulations.

	Air	Water
Density [kg/m^3]	1.185	997.0
Dynamic Viscosity [kg/m s]	1.831E-5	8.899E-4
C_P [J/kg K]	1004.4	4181.7
Conductivity [W/m K]	0.0261	0.6069

ANSYS CFX was used as the CFD package due to being a proven solver. The 2nd order high-resolution advection scheme was used due to its high accuracy. The problem is steady-state, however the CFX solver still employs "a false timestep as a means of under-relaxing the equations as they iterate towards the final solution" [52]. This improves the stability of the numerical solution, and allows for easier convergence. This timescale was controlled using the "Auto Timescale" option, which provides a conservative estimate. Because the simulations did not take very long to run (less than 1 hour), the auto timescale was preferred over a more aggressive approach, which would have decreased convergence time at the expense of numerical stability.

Two quantities were monitored to establish convergence: the pressure drop across the porous block, and the bulk temperature at the outlet. Recall that the purpose of these simulations was to find C_f, K, and h_{sf}. C_f and K are computed using the pressure drop, and h_{sf} is computed using the bulk outlet temperature. Therefore, once these two quantities are unchanging to within an acceptable tolerance, the simulation is considered resolved for this purpose. This was useful in deciding on the residual target. The root mean square residual was monitored, since it is the industry standard. It was found that by the time the residuals reached 1E-4, the two quantities of interest had stopped changing to within 2%. To decrease the error even further, the computational time required grows exponentially. For the purposes of these preliminary simulations, which was to compute the closure parameters, an accuracy of 2% was deemed adequate. The length of time taken to decrease this error percent is not worth the extra accuracy, which is why 2% was chosen. Therefore, 1E-4 was chosen as the residual target for all simulations.

The solid phase is modelled as isothermal. Therefore, the wall boundaries where the fluid phase contacts the solid phase is specified as 318K, and the bulk inlet temperature is 298K. The temperature difference was chosen for two reasons. From the CFD simulations mentioned previously in which a 1D conduction model is proposed [46], the temperature difference was the same. The same boundary conditions were used in the present work to ensure the computational set up was correct and that the simulation was run in the correct manner.

A second reason is that the temperature difference between the inlet temperature and wall temperature does not affect the interstitial heat transfer coefficient. While it is true that the temperature is used to compute the coefficient, it does not depend directly on the heating conditions. It is important to note that the heat transfer coefficient is purely a function of the local Reynolds and Prandtl number.

The energy increase due to viscous dissipation was neglected, and the boundary conditions are listed in Table 3.2.

Table 3.2: Summary of boundary conditions for isothermal simulation shown in Fig. 3.2

Surface	Boundary (no slip wall) and specified temperature of 318 [K]
Inlet	Specified mass flow and temperature of 298 [K]
Outlet	0 [Pa gauge]
Sides	Translational periodicity

Again, it is emphasized that the geometry being modeled is considered to be a REV. It follows that the geometry is sufficiently small that an isothermal condition in the solid phase is a reasonable assumption. That is also the reasoning for the periodic boundary condition – the REV is considered small enough that the bulk axial velocity is uniform and that the REV is spatially periodic. The h_{sf} for a given working fluid is purely a function of the Reynolds number for small temperature differences between the solid phase and fluid phase (20 [K] in this case). Thus, if a correlation is found for h_{sf} and Reynolds number, this can be input into the porous continuum model since a conjugate non-isothermal simulation will have varying Reynolds numbers throughout the domain (particularly in the boundary layer). A correlation would thus specify a different heat transfer coefficient at each volume, depending on the local Reynolds number. A total of 30 cases were run for each working fluid – 3 different porosities at 10 different Re each.

3.4 Grid independence

To ensure the solutions were independent of the grid density, grid-convergence simulations were performed. This involved starting with a coarse grid and then doubling the mesh size until a certain measured property stayed within some predetermined tolerance. The two measured quantities were the pressure drop across the porous block, and the bulk outlet temperature. These parameters were measured due to their physical relevance - as stated previously, the closure parameters depend only on these quantities, and so once they are unchanging, the simulation is considered grid independent for this purpose. Table 3.3 below shows the quantities computed using 3 different meshes. It is standard practice to use the "worst case scenario" when running a grid independence study – that is, the study is run using the case that would have the most difficulty converging. Following this, the grid independence study was performed using a porosity of 0.75, pore diameter 400 microns, water, and Re 200.

Table 3.3: Summary of measured quantities showing improved accuracy as a result of increasingly fine mesh used in isothermal simulations

	Elements	Pressure drop [Pa]	|% diff|	Q [W]	|% diff|
Mesh 1	1750000	20036.75		18.57	
Mesh 2	3500000	17824.34	12.41	22.13	16.09
Mesh 3	7000000	17097.78	4.25	21.27	4.04

The solution remains within 5% of the coarser mesh, and so is considered converged. The final mesh has ~630000 nodes and ~3500000 elements. Meshing was performed using ANSYS mesher and tetrahedra were chosen as the element shape due to being the standard in computational fluid dynamics for irregular geometries. Figure 3.3 shows the mesh used for a sample geometry. 5% was chosen as the criteria for grid convergence since a mesh doubled in size of mesh 3 is much more computationally expensive, and the extra accuracy gained is not worth the computational cost due to the large number of simulations that must be performed.

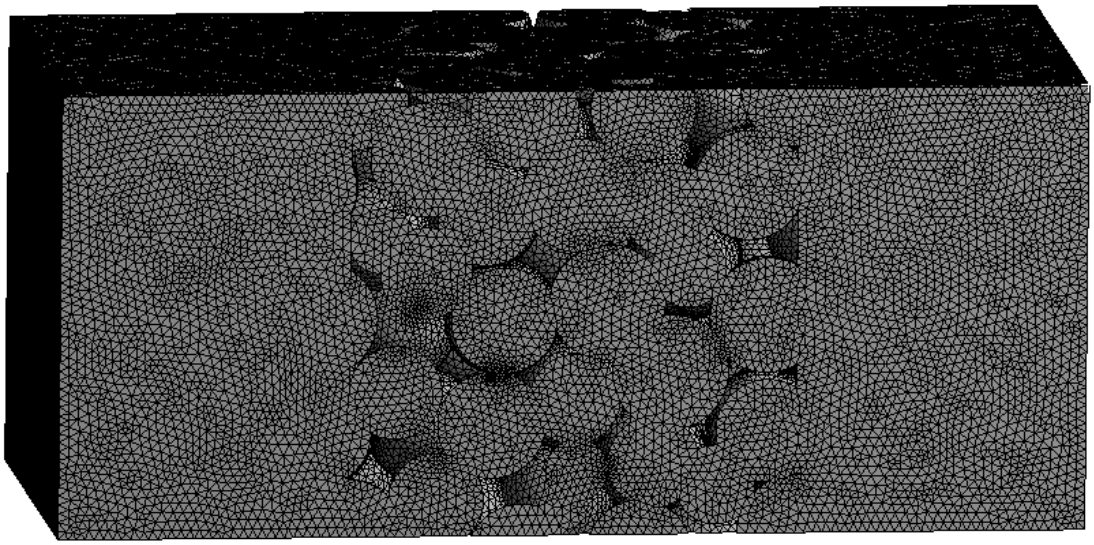

Figure 3.3: Mesh used for preliminary isothermal simulations (Porosity 0.85 is shown)

3.5 Results

Table 3.4 below shows the results and computed parameters for a single geometry and working fluid – in this case, porosity 0.85, pore diameter 400 microns, and water as the fluid. The following sections will detail how these parameters were computed.

Table 3.4: Summary of computed parameters

Re	Inlet Velocity [r	Mass flow rate	Pin [Pa]	Pout [Pa]	Delta P	dP/dX	Tout [K]	hsf
1	2.23E-03	5.30E-06	2.03E+00	9.24E-03	2.02E+00	1.31E+03	3.18E+02	7.36E+03
5	1.12E-02	2.65E-05	1.06E+01	-1.91E-03	1.06E+01	6.90E+03	3.17E+02	1.14E+04
10	2.23E-02	5.30E-05	2.31E+01	-1.39E-01	2.32E+01	1.51E+04	3.15E+02	1.37E+04
15	3.35E-02	7.96E-05	3.79E+01	-4.27E-01	3.83E+01	2.49E+04	3.13E+02	1.54E+04
20	4.46E-02	1.06E-04	5.52E+01	-8.78E-01	5.60E+01	3.64E+04	3.11E+02	1.67E+04
40	8.93E-02	2.12E-04	1.51E+02	-4.33E+00	1.55E+02	1.01E+05	3.08E+02	2.00E+04
80	1.79E-01	4.24E-04	4.77E+02	-1.88E+01	4.96E+02	3.22E+05	3.05E+02	2.39E+04
120	2.68E-01	6.36E-04	9.90E+02	-4.22E+01	1.03E+03	6.71E+05	3.03E+02	2.63E+04
160	3.57E-01	8.49E-04	1.69E+03	-7.58E+01	1.77E+03	1.15E+06	3.02E+02	2.78E+04
200	4.46E-01	1.06E-03	2.60E+03	-1.10E+02	2.71E+03	1.76E+06	3.02E+02	2.87E+04

3.5.1 Momentum results

The Forcheimer constant and permeability can be found using the pressure drop across the porous block. The coefficients K and C_f are determined by the expression shown in equation (3.1):

$$\frac{\Delta P}{L} = \frac{\mu}{K} U + \frac{\rho C_f}{\sqrt{K}} U^2 \tag{3.1}$$

This is the extended Darcy Law, where the second term on the RHS accounts for the inertial effects. The L in the equation refers to the lateral width of the porous block, since ΔP is the pressure drop across the block. K and C_f are used as closure parameters in the volume averaged equations, and are essential to modeling an accurate pressure drop. The area-weighted average pressure is computed at both the inlet and outlet of the porous block, shown as surfaces in Fig. 3.4.

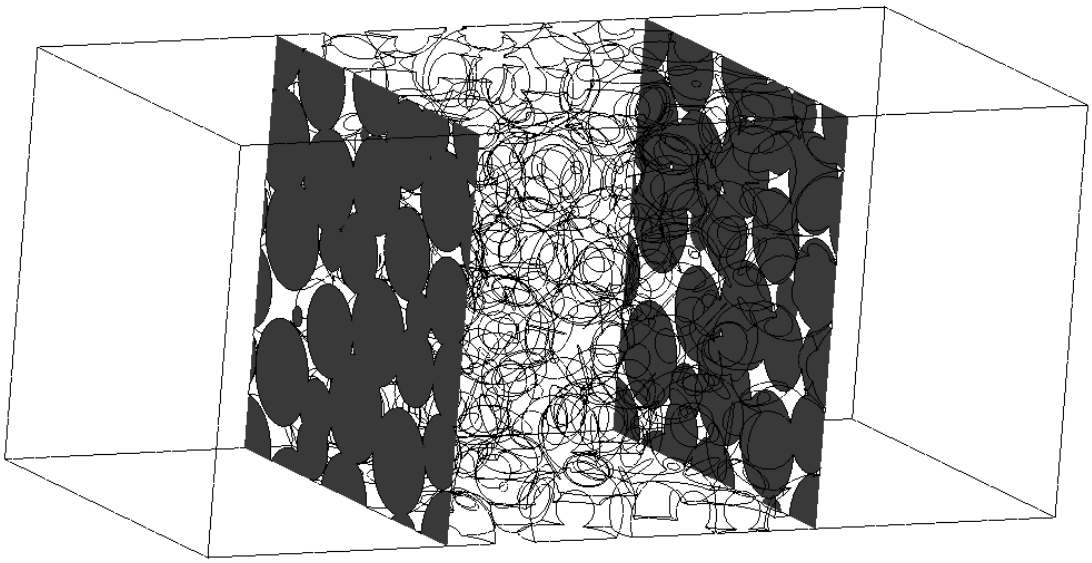

Figure 3.4: Inlet and outlet surfaces of porous block

Eq. (3.2) shows the expression used to compute the area-weighted average. At each node, the quantity (pressure in this case) is multiplied by the cross-sectional area of that volume. The entire surface is summed, and then divided by the total area. The area

weighted average was used for pressure since it made the most physical sense – pressure multiplied by area is force, and there must be a force balance throughout the domain.

$$\frac{1}{A}\int \varphi dA = \frac{1}{A}\sum_{i=1}^{n} \varphi_i |A_i| \tag{3.2}$$

Once the pressures are computed, the quantity dP/dx (or $\Delta P/L$) can be plotted for all cases considered. This is shown in Fig. 3.5, where $\Delta P/L$ is a function of the inlet velocity.

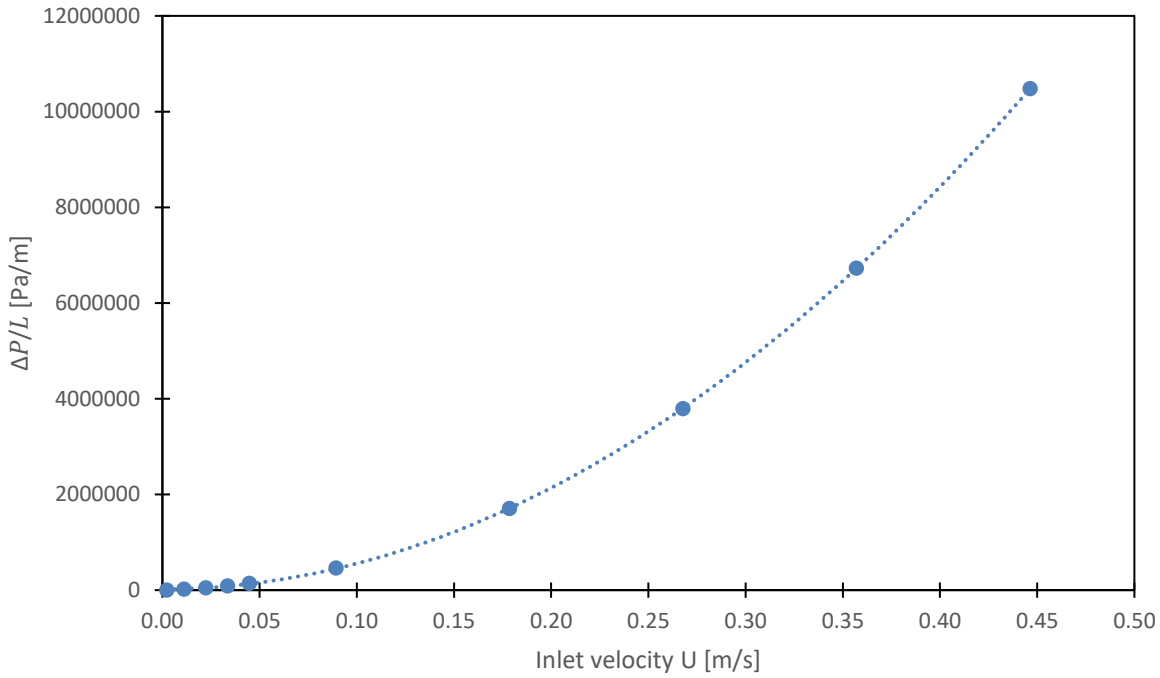

Figure 3.5: Pressure drop across porous block as a function of inlet velocity.

At low values of U, the second term on the RHS of Eq. (3.1) is negligible, and there is a linear relationship between the inlet velocity and the pressure drop. However, as U increases, this term becomes more significant, and the relationship blends into a parabola. One method of finding the two parameters is to use the first few data points in the linear range to compute the permeability first, then use the remaining data points to compute the Forcheimer coefficient. Another more streamlined process simply fits a quadratic curve to all data points throughout the range of Reynolds numbers, and from there the quadratic

equation can be used to calculate the permeability K and the Forcheimer coefficient C_f. This was the approach taken by Dyck [38], and was shown to be equally valid. Table 3.5 shows the computed K and C_f for at different geometries and working fluids. The velocity vector contours taken from a sample simulation at the y = 0 plane are also shown in Fig. 3.6. The effects of the void phase in the porous structure can clearly be seen even at low Reynolds number – the velocity field leads to greatly enhanced mixing when compared to a common structure such as fins or cylinders in usual heat sinks. It should be noted that there are also dead areas – area in which the pores are not open, and the fluid does not flow through, indicated by a darker shade of blue in the contour plot. This is a result of the geometry generation process. In real life application, the forming processes sometimes create these dead areas as well.

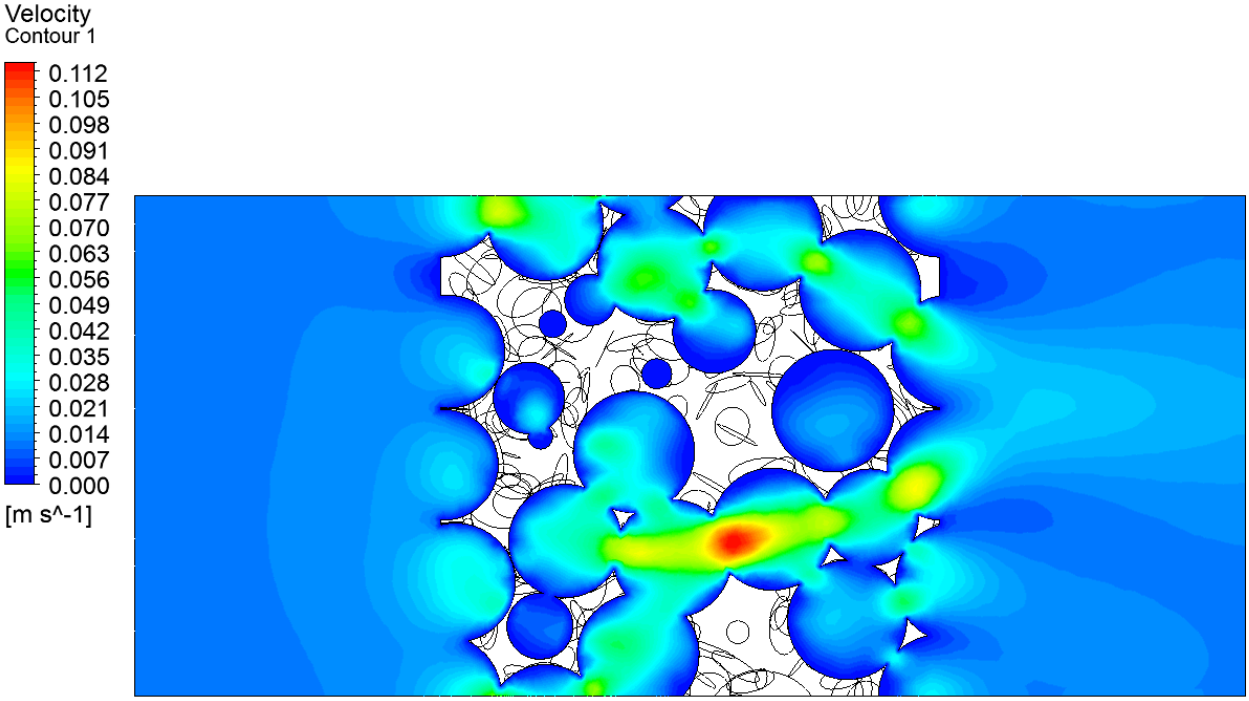

Figure 3.6: Velocity vector contours at Re 5, Porosity 0.75, Water, isothermal case, from y = 0 plane

Table 3.5: C_f and K at different geometries

Diameter	Porosity	Fluid	K	C_f
400	0.75	Air	1.09E-09	0.46
400	0.8	Air	1.44E-09	0.41
400	0.85	Air	2.62E-09	0.40
400	0.75	Water	7.00E-10	1.08
400	0.8	Water	1.09E-09	0.47
400	0.85	Water	1.69E-09	0.26
800	0.7	Water	2.67E-09	1.42
800	0.8	Water	5.00E-09	0.40
800	0.85	Water	7.96E-09	0.24

3.5.2 Thermal results

Figure 3.7 shows the temperature contours at Re = 5 taken from the y = 0 plane. The fluid quickly approaches the solid phase temperature, even at high flow. Recall that the isothermal case is treated as an REV. Since the ΔT between the solid and fluid phase is small enough that the fluid properties remain constant, h_{sf} is not a function of temperature, and is a function of the local Reynolds number only (at a given working fluid). This is the reasoning for finding the interstitial heat transfer coefficient at different Reynolds numbers – once a function is found that relates the coefficient to the local Reynolds number, this function can be used in fully conjugate simulations where the velocity is not uniform as it is in the isothermal case (due to the periodic boundary conditions).

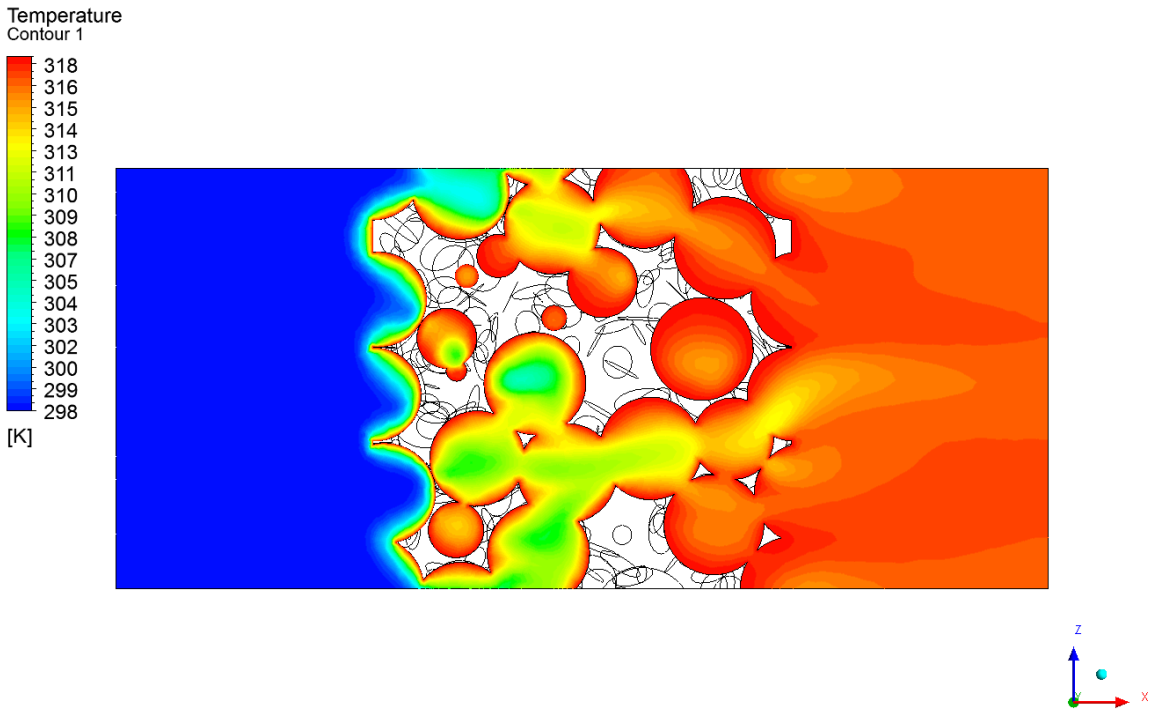

Figure 3.7: Temperature contours at Re 5, Porosity 0.75, Water, isothermal case, from y = 0 plane

The interstitial heat transfer coefficient is found by using an equation analogous to heat transfer in heated pipe flow. For a pipe with a constant wall temperature, the convective heat transfer is calculated using one of two expressions below:

$$Q_{conv} = \dot{m}C_p(\Delta T_i - \Delta T_o); where\ \Delta T_m = T_w - T_m \tag{3.3}$$

$$Q_{conv} = hA_s\Delta T_{LM} \tag{3.4}$$

$$log\ mean\ temperature\ difference\ \Delta T_{LM} = \frac{\Delta T_o - \Delta T_i}{\ln\left(\frac{\Delta T_o}{\Delta T_i}\right)} \tag{3.5}$$

By equating the two heat transfer expressions, the following equation arises to calculate the heat transfer coefficient:

$$h = \frac{-\dot{m}C_p \ln\left(\frac{\Delta T_o}{\Delta T_i}\right)}{A_s} = \frac{-\dot{m}C_p \ln\left(\frac{T_w - T_o}{T_w - T_i}\right)}{A_s} \tag{3.6}$$

This equation can be readily applied to porous media. In the case of an isothermal solid region, the constant wall temperature is the uniform solid temperature. Instead of A_s, the surface area of a pipe, the surface area of the porous geometry is used instead, A_{sf}, which can easily be found in SolidWorks. T_w is the uniform temperature of the solid (the wall temperature 318 [K]), T_i is the specified inlet temperature (298 [K]), and T_o is the bulk outlet temperature. The interstitial heat transfer coefficient in a porous material with constant solid temperature is therefore:

$$h_{sf} = \frac{-\dot{m}C_p \ln\left(\frac{T_w - T_o}{T_w - T_i}\right)}{A_{sf}} \tag{3.7}$$

To find the bulk outlet temperature T_o, a mass weighted average of the temperature is computed at the outlet surface (shown in Fig. 3.8).

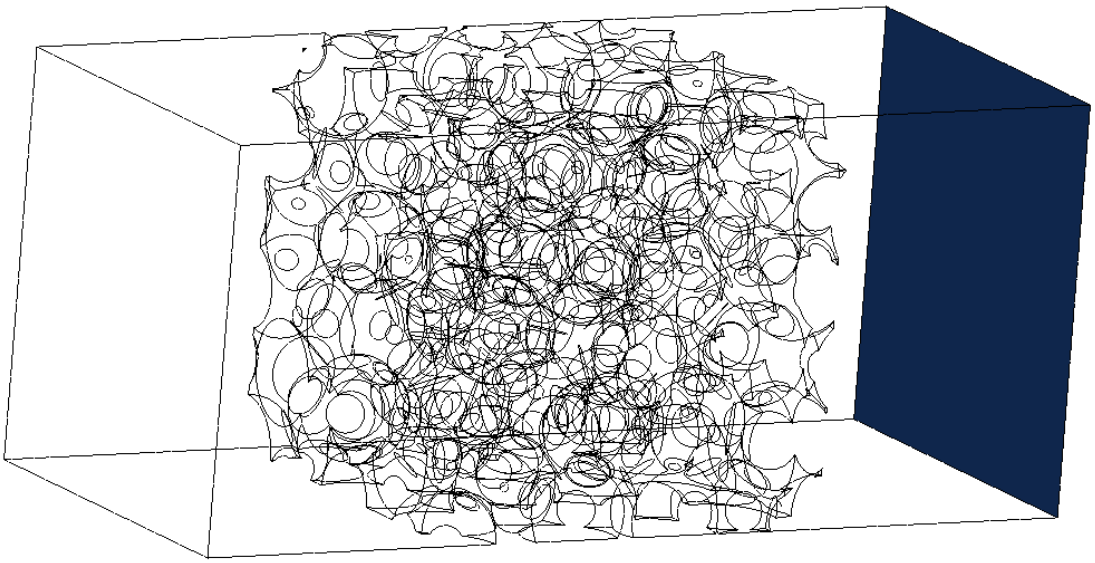

Figure 3.8: Outlet surface of computational domain over which bulk outlet temperature is found (note that the outlet is entirely a pure fluid region).

The equation CFX used to calculate the mass-weighted average is shown in Eq. (3.8). Similar to the area weighted average, at each node the quantity (temperature) is multiplied by the mass flow rate over the boundary face. The entire surface is summed in this fashion, then divided by the total mass flow rate through the surface. The mass weighted average was used instead of the area weighted average because of its physical relevance – energy requires mass, and whenever an energy balance is performed, the temperature is always multiplied by the mass flow rate.

$$\frac{\int \varphi\rho\left|\vec{v}\cdot d\vec{A}\right|}{\int \rho\left|\vec{v}\cdot d\vec{A}\right|} = \frac{\sum_{i=1}^{n} \varphi_i\rho_i\left|\vec{v}\cdot \vec{A}\right|}{\sum_{i=1}^{n} \rho_i\left|\vec{v}\cdot \vec{A}\right|} \tag{3.8}$$

Once T_o is found, the h_{sf} at each Reynolds number can be computed. Using the pore diameter as the characteristic length, the Reynolds number is calculated as:

$$Re_d = \frac{\rho U d}{\mu} \tag{3.9}$$

Fig. 3.9 shows the variation of h_{sf} vs. Reynolds number for porosity 0.75, and water. The data points can be fit using a simple power law. This is the same form that Straatman et al. [19] used, in which the Nusselt number can be correlated as a function in the form $Nu = CPr^n Re^m$.

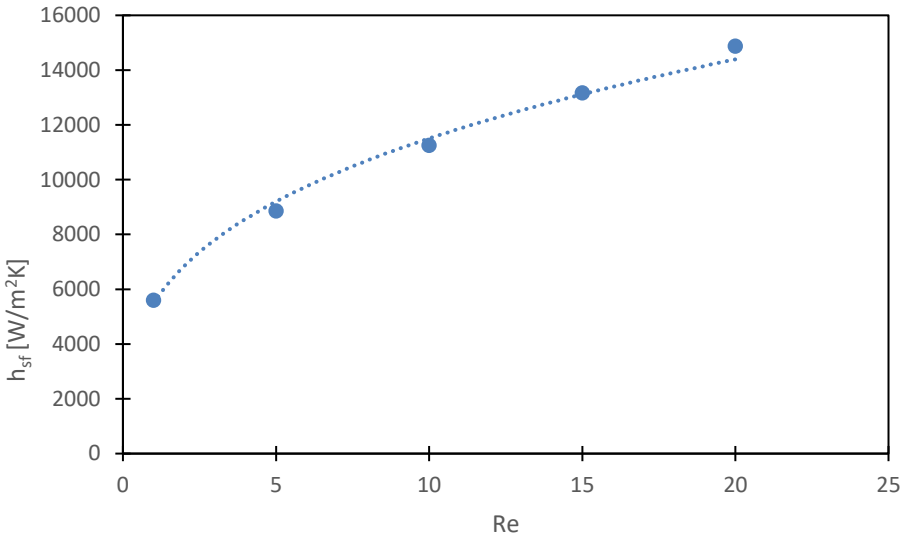

Figure 3.9: Interstitial heat transfer coefficient computed for porosity 0.75 using water as the working fluid.

Note that even though the Nusselt number is both a function of the Prandtl number and Reynolds number, a value for the n parameter (the exponent of the Prandtl number) was not computed. This was due to only using two fluids – air and water. As such, when the correlation is used in the code, a simple power law was used relating the Reynolds number to the interstitial heat transfer coefficient. In this case, the Prandtl number is constant, and so can be lumped into the C term. This correlation is now input into the porous continuum model. It is noted that the h_{sf} is much higher than that predicted by a unit cube model. To better illustrate this, consider Fig. 3.10 which shows a comparison between the unit cube model and the current geometry. Fluid will pass through the void phases in each structure. The unit cube model has a uniform and structured pattern to the void phases, as opposed to the current geometry which is much more random, and has pockets and holes of varying sizes and diameters. The randomness and varying sizes of holes in the structure leads to better mixing, and thus a much higher heat transfer coefficient.

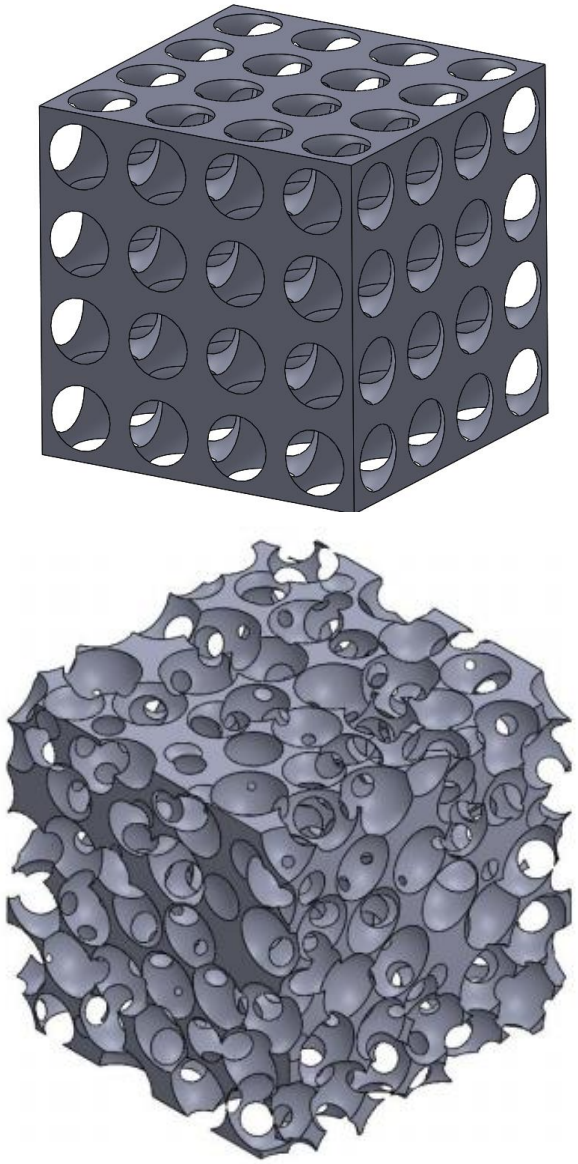

Figure 3.10: Images showing difference between unit cube model and current geometric model produced by YADE.

3.5.3 Implementation of parameters into porous continuum model

As the main purpose of the simulation work was to identify gaps and inaccuracies in porous continuum modelling, the parameters derived from the pore-level simulations were applied to the porous continuum model and for the case considered in the previous

section, cases were run and compared. It was important to validate the computed parameters, and to ensure that the method for computing them led to accurate results.

The modelling of a REV was chosen since it was the simplest possible case. The same boundary conditions and geometry dimensions are implemented into the code. Grid independence was performed, and will be detailed in a later chapter. The computed closure parameters (C_f and K) as well as the h_{sf} correlation, are input into the code. Since heat transfer is the focus, the quantity q (the heat transfer into the domain) is compared between the two simulations. This is calculated using an earlier equation mentioned:

$$Q_{conv} = \dot{m} C_p (T_o - T_i) \tag{3.10}$$

Table 3.6 below shows the comparison at porosity 0.75 and 400 microns, with water. From Re 1 to 200, there is less than 5% difference between the two results, giving confidence in the method and equations used to calculate these parameters. The percentage error (calculated by $100*(Q_{pore\text{-}level}-Q_{continuum})/ Q_{pore\text{-}level}$) does not follow any trend based on Reynolds number.

Table 3.6: Comparison of heat transfer in isothermal case between pore-level simulations and porous continuum simulations

Q [W]			
Re	Pore-level	Porous continuum	% diff
1	0.496	0.501	0.972
5	2.326	2.405	3.396
10	4.114	4.124	0.255
15	5.568	5.682	2.057
20	6.837	7.076	3.49
40	10.866	11.255	3.581
80	15.801	16.262	2.917
120	18.513	18.616	0.627
160	20.174	20.599	2.105
200	21.238	21.763	2.473

Figures 3.11 and 3.12 show the bulk axial pressure and temperature, respectively. From these plots, not only does the bulk heat transfer match to within 5%, but the temperature and pressure profiles match to within 5% as well which indicates that it is now safe to

proceed to the conjugate simulations. The solid red line shows the pressure obtained from pore level simulations (CFX) while the blue dots indicate the results taken from the volume – averaged (VA) code (the porous continuum model). The pressure profile taken from CFX was an area-weighted average pressure in the axial direction, taken at discrete points. Once plotted, these points are connected – hence why the pressure profile is not a smooth line, and has "wiggles" appearing.

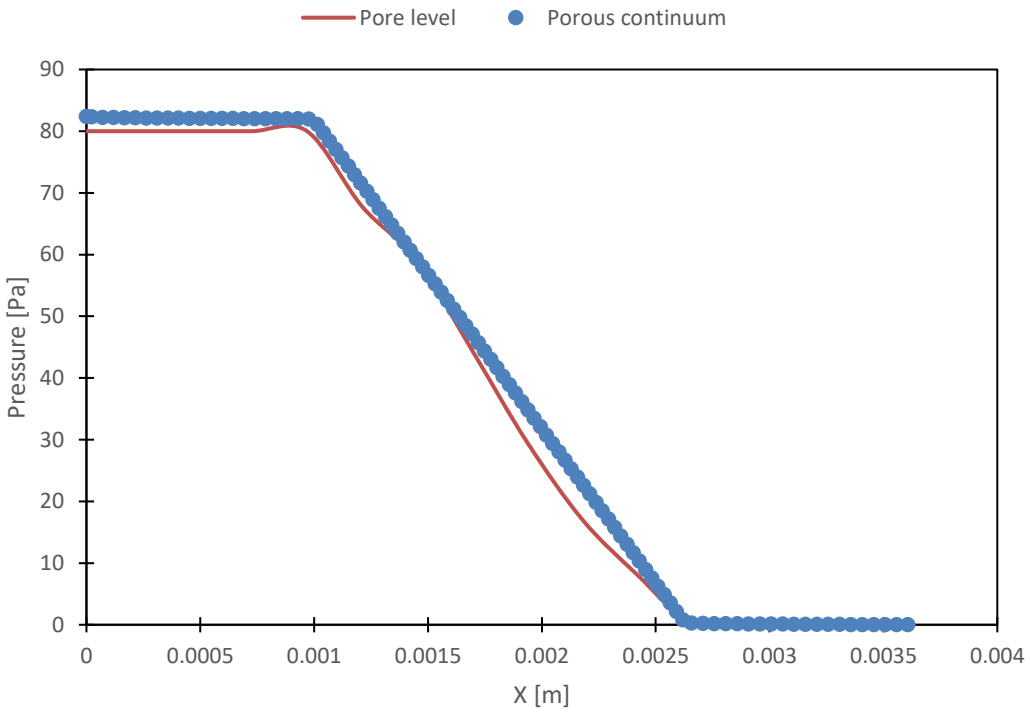

Figure 3.11: Axial pressure drop for porosity 0.75, water, Re 10, isothermal case

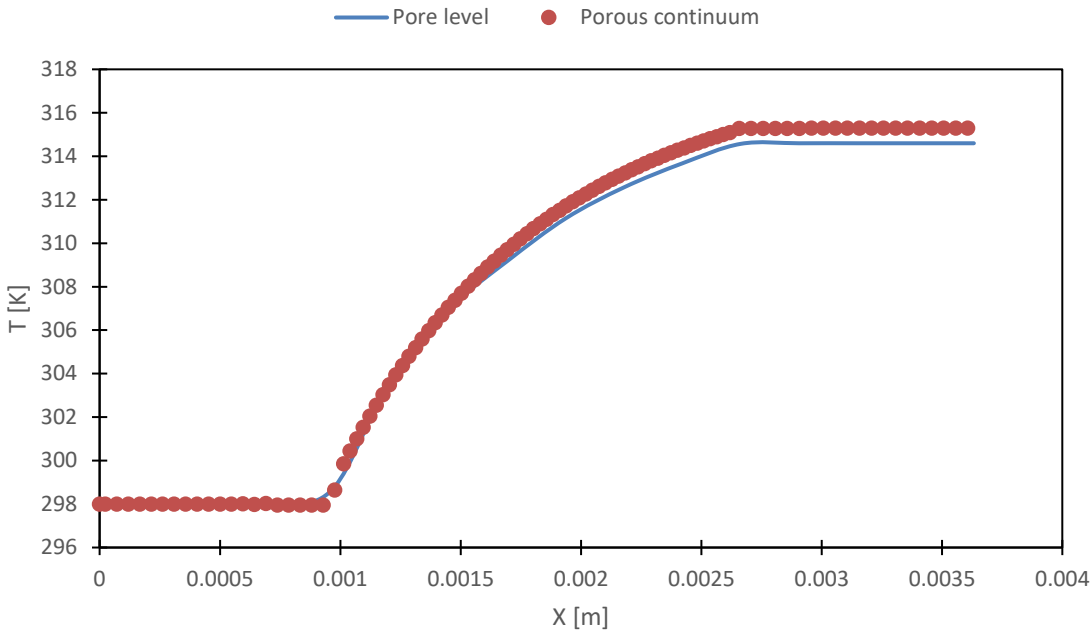

Figure 3.12: Axial bulk temperature for porosity 0.75, water, Re 10

3.6 Summary

This chapter detailed the preliminary CFD simulations performed to compute the closure parameters required before solving the volume-averaged governing equations: the Forcheimer coefficient C_f, the permeability K, and the interstitial heat transfer coefficient h_{sf}. A correlation was developed which computes the h_{sf} based on the local Reynolds number and Prandtl number. 3 different geometries were used: porosity 0.75, 0.80, and 0.85 all at a pore diameter of 400 microns. ANSYS CFX was used as the commercial CFD software, and the results were grid independent to within 5%. Validation was performed which gives confidence in the method used to calculate the parameters.

Chapter 4

4 Conjugate simulations

4.1 Introduction

One of the purposes of the volume-averaged 3D code is to provide a computationally efficient, yet still accurate, substitute to pore level simulations. In applications such as the design of heat sinks, this decreased simulation time is extremely valuable. When heat sinks are modeled, generally the isothermal assumption is not applicable, and so a full conjugate domain must be used – where both the fluid phase and the solid phase temperatures are solved. This becomes very computationally expensive when solving the instantaneous Navier-Stokes equations on a geometry such as the one generated in previous sections. An alternative is to solve the volume-averaged equations instead, which is what the porous continuum model does using a finite volume method. Once the closure parameters have been obtained from the preliminary pore-level simulations, they can be input into the porous continuum model. If the porous continuum model can provide a reasonably accurate representation of the pore level conjugate physics, this will be of great benefit in design processes due to the faster simulation time. This chapter will detail the comparisons, and the major differences, between the pore level and volume averaged conjugate simulations.

4.2 Geometry

Since the conjugate simulation no longer has the isothermal condition, the solid phase must be modeled and meshed as well. The geometry for a conjugate simulation is therefore the same as the isothermal case, however with the addition of the solid phase. Both the solid and fluid phase are mated together to form a conjugate geometry. This can be seen in Fig. 4.1. The same geometry specifications were used: 3 different porosities at 0.75, 0.80, and 0.85, and 2 different pore diameters at 400 microns and 800 microns.

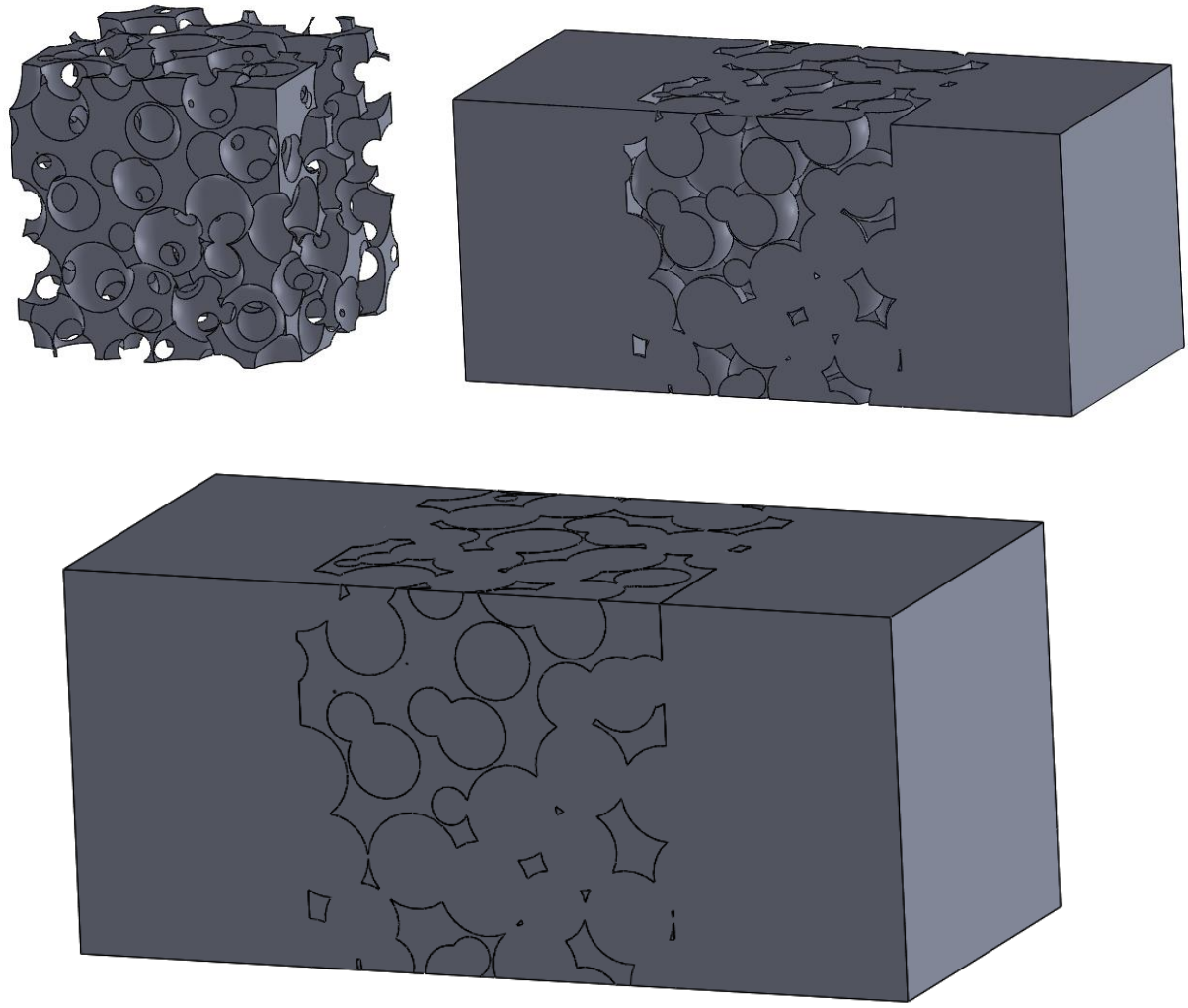

Figure 4.1: CAD model of geometry used for conjugate simulations. Top shows solid and fluid geometry before mating. Bottom shows final geometry.

4.3 Computational set up of pore-level model

The same solver settings were used as in the isothermal case. However, the boundary conditions (shown below in Table 4.1) are slightly different to mimic a case wherein the porous region is heated from below by a substrate. This case was chosen due to being the standard application for heat sinks – for example in finned heat sinks with porous materials in between the fins [52].

Table 4.1: Summary of boundary conditions for conjugate simulation shown in Fig. 4.1

Bottom	No slip wall and specified temperature of 318 [K]
Top	No slip wall and adiabatic
Fluid/Solid interface	Interface condition
Inlet	Specified mass flow and temperature of 298 [K]
Outlet	Opening and 0 [Pa]
Left/Right side	Symmetry

Instead of a uniform temperature for the solid, a temperature of 318 [K] is specified on the bottom surface of the porous block – at both the fluid and the solid phases. This is more realistic, and similar to how heat sinks are used in real world applications. The periodic boundary conditions no longer apply – instead, the left and right sides are specified as symmetry, and the top is adiabatic. These were chosen, again, to closely resemble heat sinks in real applications. At the fluid/solid interface, an interfacial condition was specified which allows for heat transfer between the two surfaces. This was needed due to the local thermal non-equilibrium. The properties of Aluminum were specified for the solid material. Due to its high conductivity, it is a favored material for porous materials in enhanced heat transfer applications (other popular choices being graphite and carbon). However, for the purpose of this work, it should be noted that the material of the solid phase is of little consequence. For one, the conductivity of a material can be changed through heat treatment [53]. Secondly, the present work aims to investigate the *differences* between the results generated by the porous continuum model and those generated by commercial CFD software. The actual operating conditions are of little significance, and only the differences are noted.

4.4 Grid independence

The grid independence was carried out in the exact same way as the isothermal case. Table 4.2 below shows the convergence of the quantities of interest, using water at Re 200, porosity 0.75, and 400-micron pore diameter.

Table 4.2: Summary of measured quantities showing improved accuracy as a result of increasingly fine mesh used in conjugate simulations

	Elements	Pressure drop [Pa]	|% diff|	Q [W]	|% diff|
Mesh 1	3,250,000	20155.75		6.23	
Mesh 2	6,500,000	18124.60	10.08	5.70	8.54
Mesh 3	13,000,000	19031.80	5.01	5.82	2.09

The final mesh for the non – isothermal simulations had ~1,250,000 nodes and ~6,500,000 elements. Figure 4.2 shows the mesh used in the non – isothermal case. The tolerance for grid convergence was set at 5%. A mesh finer than 13,000,000 took much longer to run than one at 6,500,000, and the accuracy was deemed not worth the extra time.

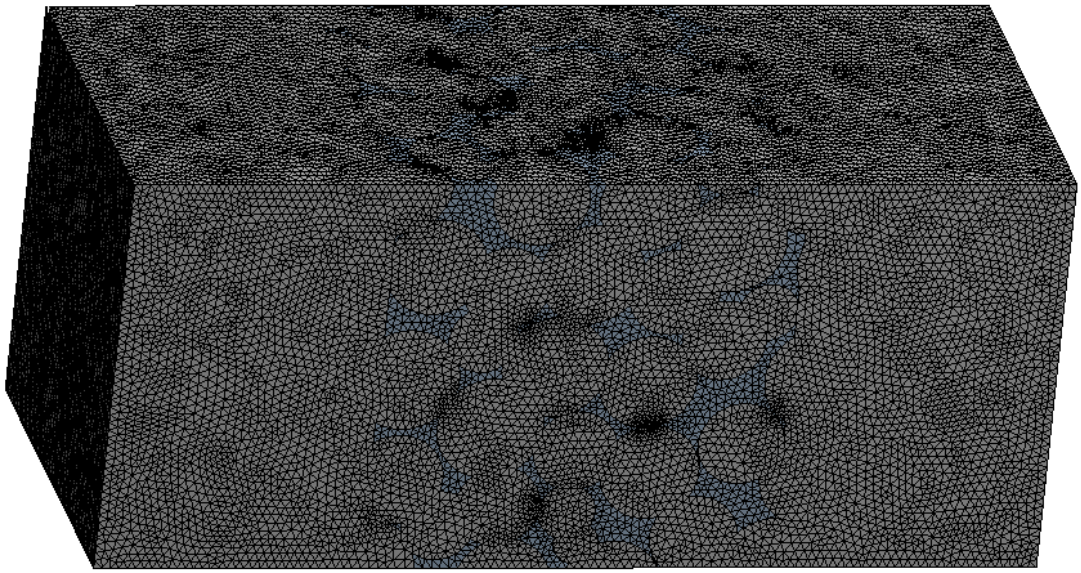

Figure 4.2: Mesh used in conjugate simulations (Porosity 0.85 is shown)

4.5 Computational setup of volume averaged model

The closure parameters obtained in Chapter 3 are input into the porous continuum model. The boundary conditions are the same as those used for the pore level simulation. Thermal dispersion was modelled using a correlation developed by Calmidi et al for aluminum foams [26]. This was chosen due to the same material being used, as well as

results appearing reasonable. The dispersion conductivity is calculated by equation (4.1) shown below:

$$\frac{k_d}{k_e} = 0.06 Re_K Pr_e \qquad (4.1)$$

where Re_K is the Reynolds number based on permeability and Pr_e is the Prandtl number based on the effective conductivity of the porous medium k_e. The steady state solutions were obtained for the range of Reynolds numbers, and using air and water. On average, both the energy and momentum equations were converged to a mean residual of less than 1E-10.

4.5.1 Grid independence in continuum model simulations

A grid independence study was also carried out on the volume averaged cases, and the mesh is shown below. It was found that 105 nodes were needed in the x – direction, and 55 nodes in the y – direction. The z – direction (which, in this case, is the width, and not the height), only required 1 node due to the symmetry boundary condition. The final mesh is shown in Fig. 4.3.

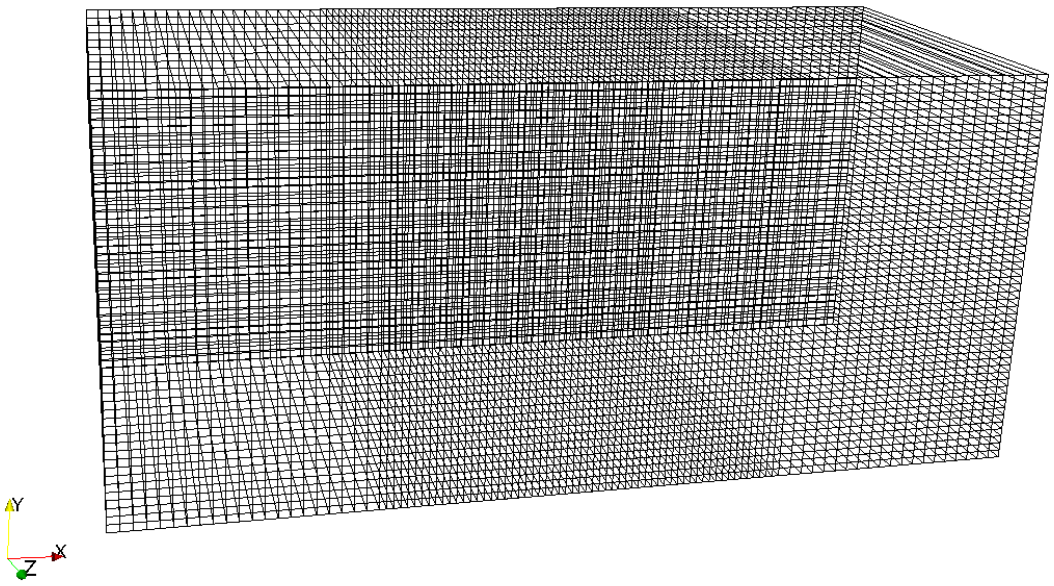

Figure 4.3: Mesh used in continuum model simulations

4.6 Results

4.6.1 Momentum results

There was very little difference in the momentum results between the isothermal and non -isothermal case, as the temperature has little influence on the velocity field. Similarly, the velocity field predicted by the porous continuum agrees well with the pore level simulations. A velocity vector contour taken at the y = 0 plane is shown in Fig. 4.4. Other than the influence of the wall boundary conditions along the top and bottom, resulting in small boundary layers, the velocity contours are very similar to the isothermal case, as indicated by the value range.

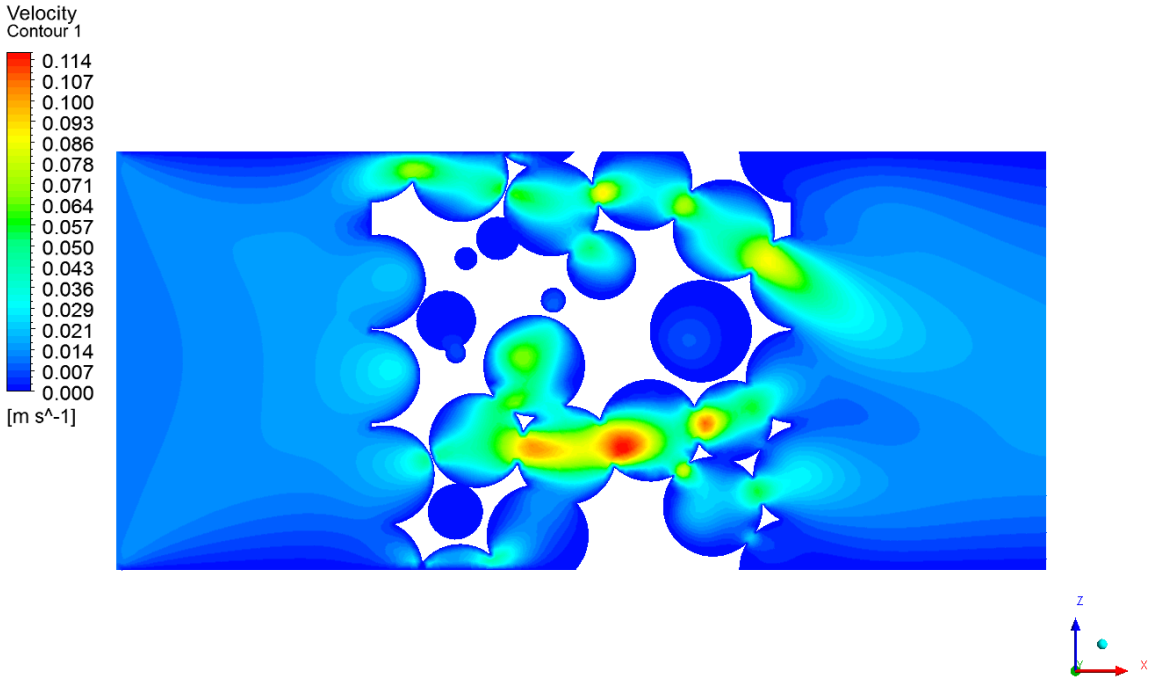

Figure 4.4: Velocity vector contours obtained from conjugate simulation at Re 5, Porosity 0.75, 400-micron diameter, and using water.

4.6.2 Energy results

The heat transfer for the conjugate system is much less than in the isothermal case – at Re 200, only a quarter of the heat is swept away in the bottom heated case (21 [W] with isothermal conditions, and 5 [W] without). The temperature contours for a sample case

are shown in Fig. 4.5, taken from the y = 0 plane. A comparison between the isothermal and non-isothermal contours show a drastic difference – even at a low Reynolds number of 5, the temperature of the solid phase quickly drops in the z-direction.

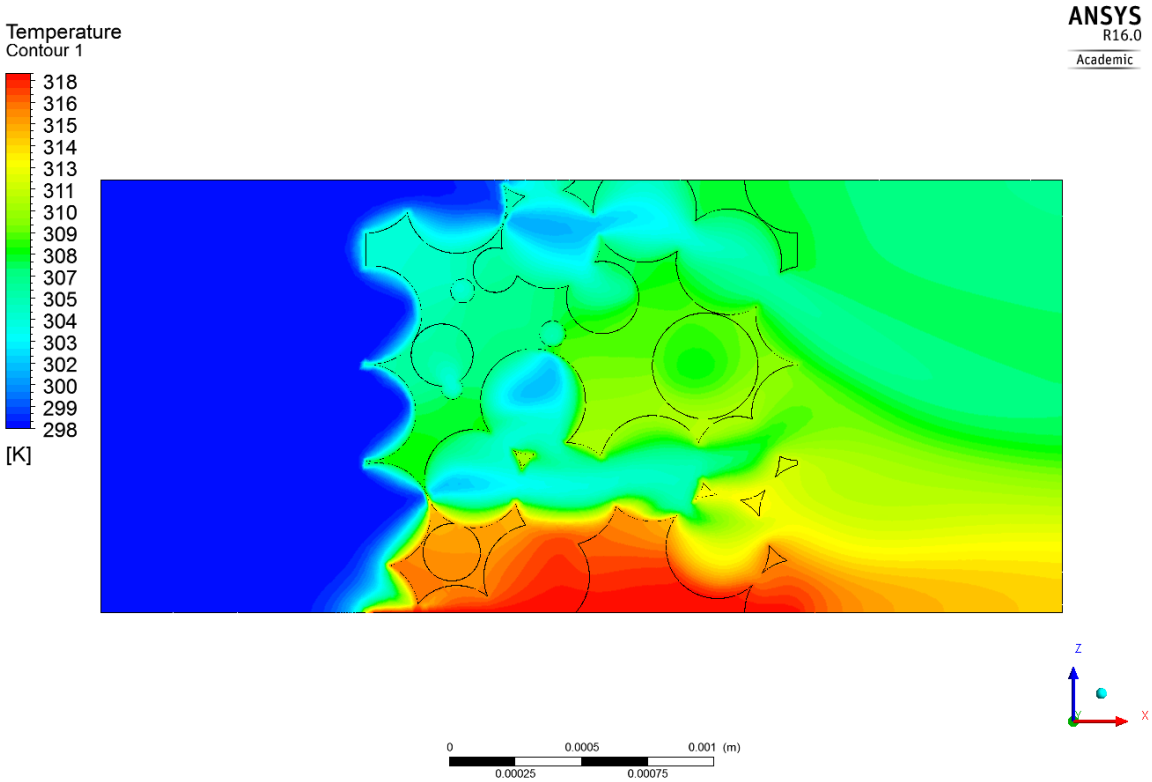

Figure 4.5: Temperature contours obtained from conjugate simulation at Re 5, Porosity 0.75, 400-micron diameter, and using water.

It is at this point that discrepancies appear between the 3D code results and the pore-level results. The total heat transfer (Q) was computed, and is plotted in Fig. 4.6 for water at porosity different porosities. The porous continuum model greatly over predicts the heat transfer with errors of up to 50% at Re 200 and using water. Using air, the magnitude of the difference is smaller, at ~20%, however this is still unacceptable. Figures 4.7 and 4.8 show the temperature contours taken at the right side of the domain – the porous continuum model predicts a much higher temperature in the boundary layer. To reconcile the differences in heat transfer predicted from the pore-level and continuum codes, two avenues are explored: the lower surface on which the temperature condition is applied, and the specification of conduction in the solid matrix.

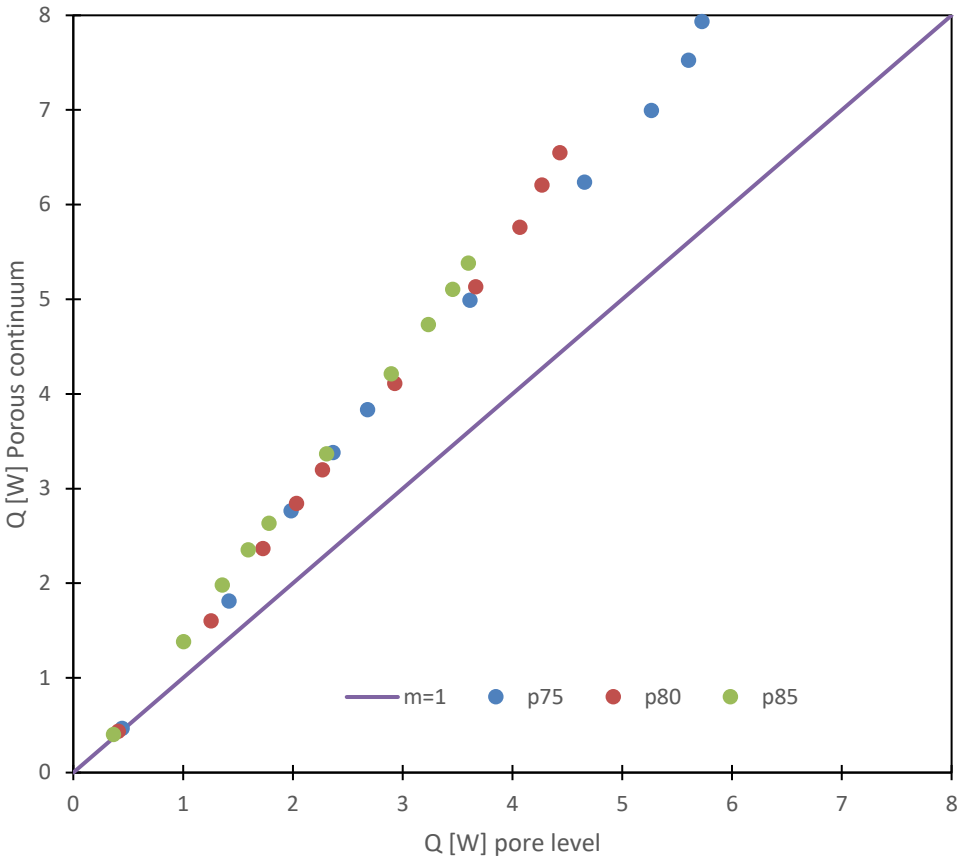

Figure 4.6: Plot showing comparisons of total heat transfer between pore – level simulation and porous continuum model.

Figure 4.7: Temperature contours obtained from porous continuum model at Re 80, Porosity 0.75, 400-micron diameter, and using water.

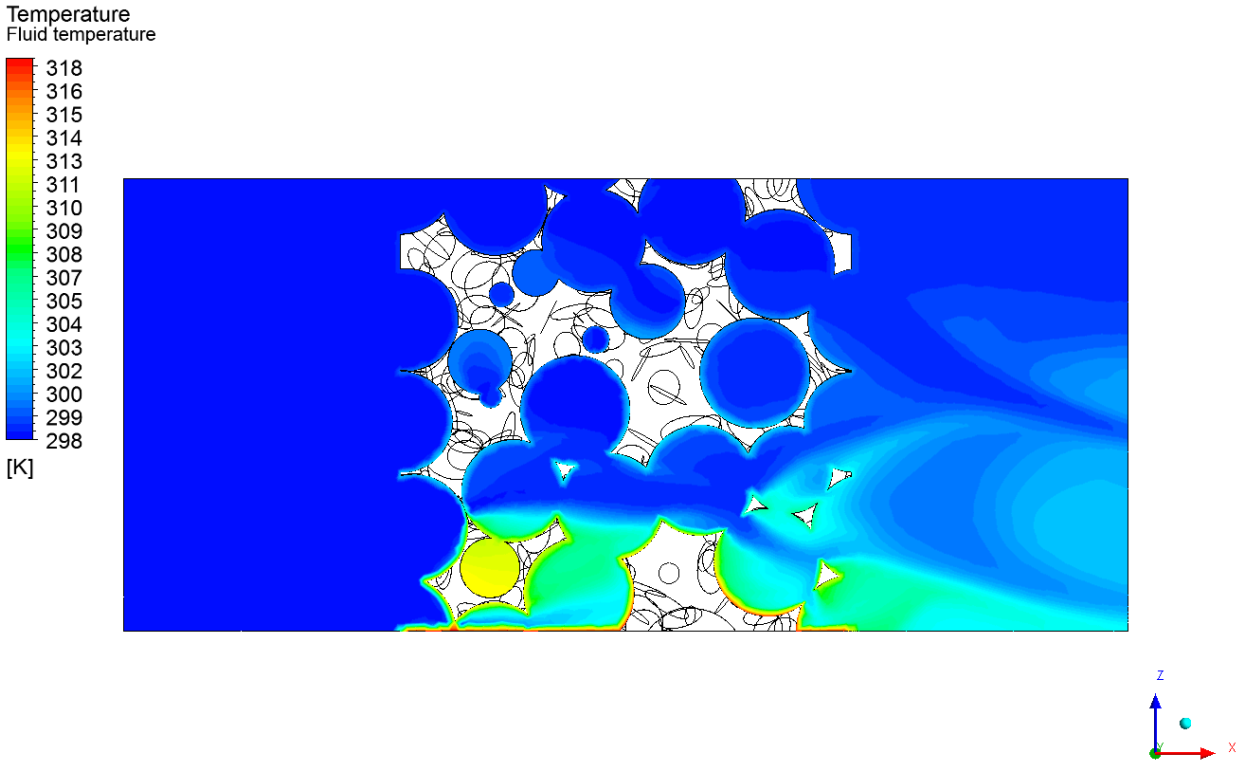

Figure 4.8: Temperature contours obtained from conjugate simulation at Re 80, Porosity 0.75, 400-micron diameter, and using water.

4.7 Full conjugate simulation with attached substrate

It was possible that the introduction of a solid substrate beneath the porous block would solve the discrepancies. Inclusion of a solid substrate at the bottom of the porous block will allow the temperature to develop towards the solid/porous interface, thereby including any resistance due to the sudden change in cross-section. The reasoning being that a Dirichlet boundary condition of a set temperature directly at the bottom was unrealistic, since this is not feasible in experiments. Rather, it is more realistic to have a substrate attached, heat the bottom, and have the resulting temperature develop naturally. Ouyang et al examined a similar effect [54] and aimed to investigate the heat transfer split at the interface between the solid substrate and the porous media zone. Instead of a set temperature, a constant heat flux was applied on the bottom. A simplified model was created from the volume averaged equations based on these boundary conditions which assumes local thermal non – equilibrium in both the substrate and the porous media zone. At the interface, the separate heat flux into the solid phase and fluid phase was compared to pore-level simulations, and was found to match closely, giving confidence in the model. For further details, and for graphs which compare quantities such as the heat flux and temperature profiles, refer to [54].

Figure 4.9 shows the geometry used for the subsequent simulations. The boundary conditions are exactly the same as the previous simulations, with the addition of a substrate. The bottom of the substrate is set to 318 [K], while the other sides of the substrate are adiabatic.

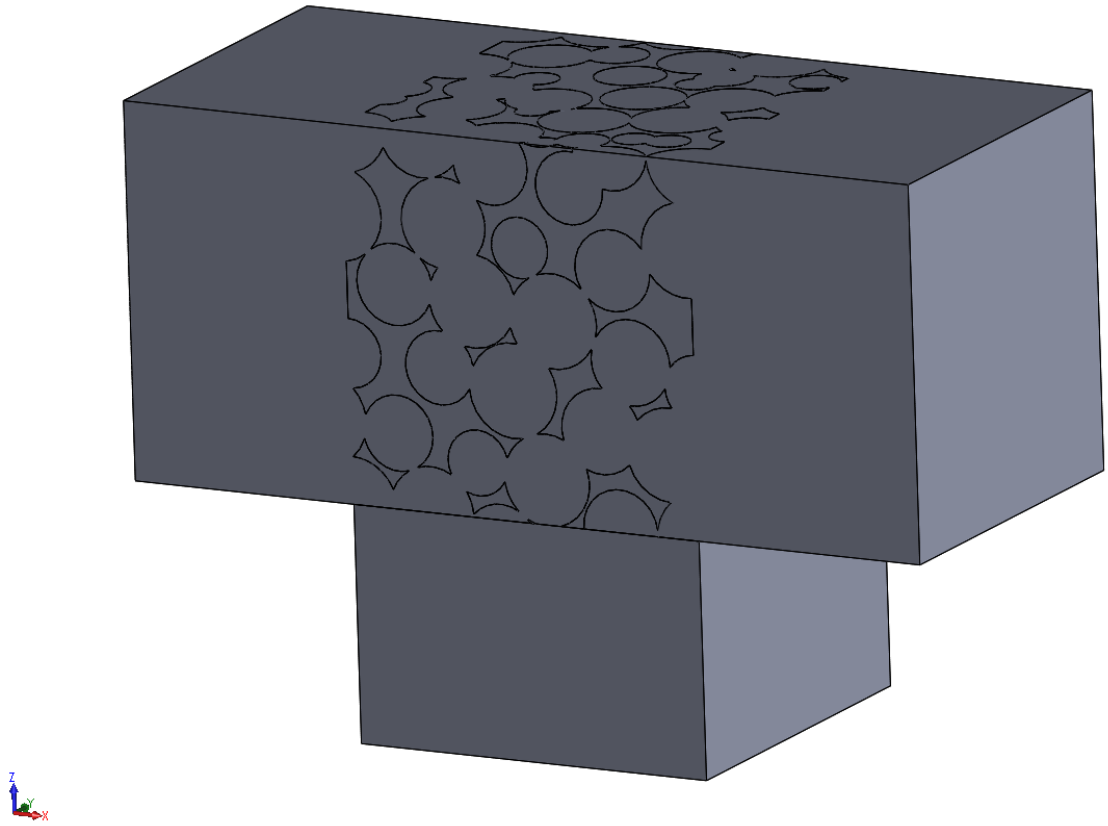

Figure 4.9: CAD model of geometry used for full conjugate simulations with substrate

4.7.1 Results

It was found that the addition of a substrate had virtually no effect on the differences between the porous continuum model and the pore level simulations – the errors were still present and of the same magnitude. Figure 4.10 shows a comparison of the temperature contours taken at the y = 0 plane between the pore level simulations heated via a solid substrate, and directly from the bottom. As observed in the work done by Ouyang et al there is a non-equilibrium region near the porous-solid interface in which the temperature profile develops. The temperature at the interface between solid and porous regions is also slightly lower than the set 318 [K] due to the increased resistance presented by the solid substrate.

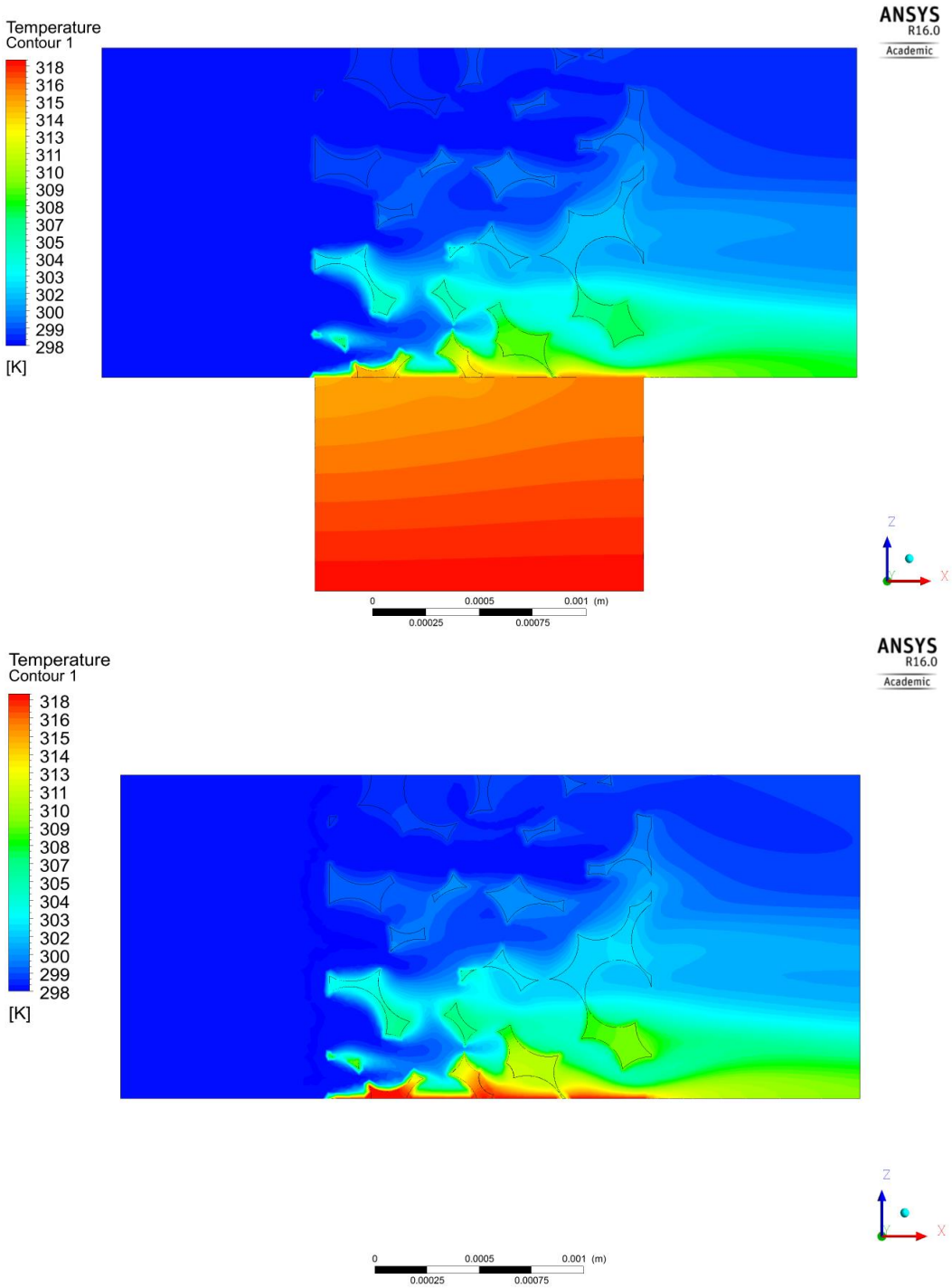

Figure 4.10: Comparison of temperature contours obtained from full conjugate simulation (top) and bottom heated conjugate simulation (bottom) at Re 20, Porosity 0.85, 400-micron diameter, and using water.

4.8 Modification of conduction within solid matrix

Another possible explanation for the discrepancy was the complex geometry of the porous material. Due to the complex path that the structure provides for heat to travel through, resistances arise which can lower the total heat transfer. This would be captured in the pore-level conjugate simulations, but not in the porous continuum code.

To test this hypothesis, a much simpler geometry using vertical solid cylinders was produced, shown in Fig. 4.11. To match the porous geometry as much as possible, the cylinder diameter, spacing, and quantity was specified in a way such that the porosity and the A_{sf} were preserved.

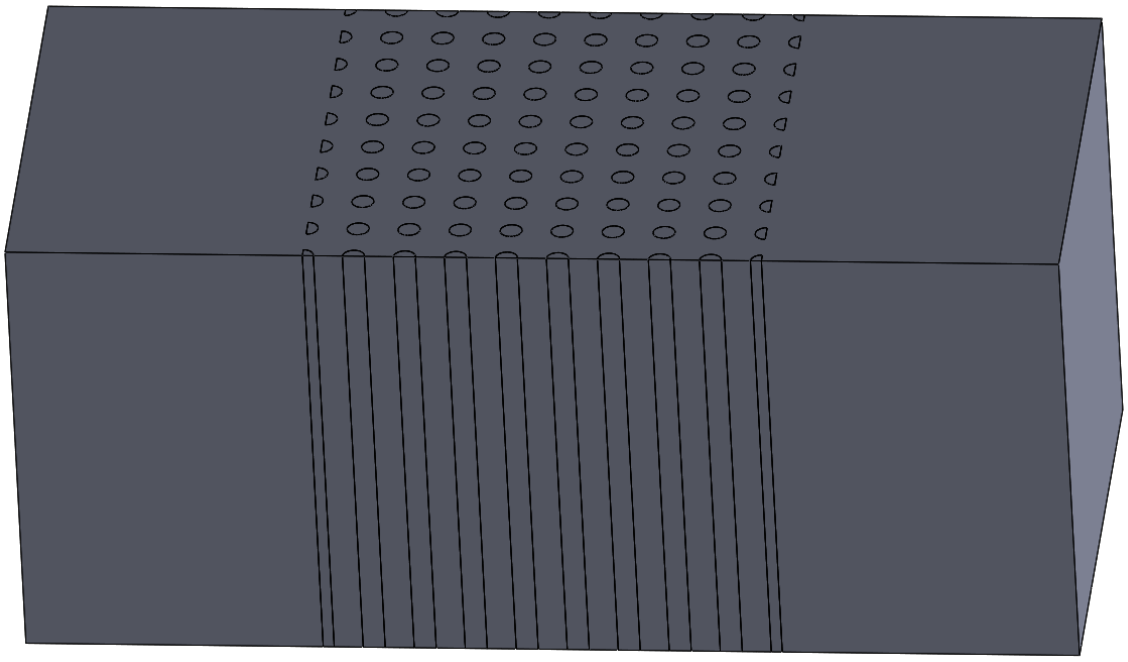

Figure 4.11: CAD model of simplified geometry used for conjugate simulation. The geometric properties (A_{sf} and porosity) were preserved from previous porous geometries.

The same procedure was used to obtain the C_f, K, and h_{sf} coefficients, and the same boundary conditions were used as in the conjugate case. Water was used as the working fluid, and aluminum properties were used for the solid material.

When comparing the results (summarized in Table 4.3) of these pore level calculations to the porous continuum model, the results were in much better agreement – the model was accurate to within 3.6%.

Table 4.3: Comparison of total heat transfer between pore level and porous continuum model using simplified geometry

Q [W]		
Pore - level	Porous continuum	% diff
0.496	0.500	0.972
2.326	2.405	3.396
4.114	4.124	0.255
5.568	5.682	2.057
6.837	7.076	3.490
10.866	11.255	3.581
15.801	16.262	2.917
18.500	18.616	0.627
20.174	20.599	2.105
21.238	21.763	2.473

This confirms the presence of a resistance caused by the complex geometry. Because the pins were straight and have a uniform cross-sectional area, the conduction path is simple. The formal name for the complexity of the porous material is referred to as “tortuosity”, which is essentially a measure of how twisting and winding a certain path length is. This property, and its implementation into the code, will be discussed in the following sections.

4.9 Calculating tortuosity

Tortuosity is typically defined as the length of the actual path, or arc length (L_C) [55], over the length of the shortest path through a porous material, or the length between two points (L).

$$\tau = \frac{L_C}{L} \tag{4.2}$$

To explain, observe the streamlines in Fig. 4.12. They do not follow a straight path – due to the cylinders placed in the field, the streamlines follow a more twisted path. The total

length of the streamline path, divided by the straight length of the rectangular geometry, is tortuosity the tortuosity factor τ. As such, the tortuosity is always greater than or equal to 1. An analogy can be made to solid conduction – Fig. 4.13 shows the conduction path in the solid phase of the porous material. Rather than streamlines, the black lines indicate the path along which conduction occurs. The lengthened conduction path presented by the geometry lessens heat transfer when compared to a straight conduction path. Along with the lengthened conduction path presented by the geometry, the tortuosity accounts for other geometric resistances such as the changing cross-sectional areas, or regions where the ligaments of the structure expand or contract in spherical void-phase porous materials. This is not shown explicitly in Eq. (4.2) since that expression is the most convenient physical expression for tortuosity, and is used in a general sense, applicable to all geometries.

It is emphasized that the tortuosity in this work focuses on the *solid* phase, not the fluid phase. The tortuosity in this work is related to the conduction path – due to the complexity of the solid structure; the conduction path is a winding and tortuous length. It is purely a function of the solid geometry, and is independent of the flow field. Kopanidis et al. [39] presented an equation used to calculate the tortuosity, however this was only applicable to Kelvin cell geometries, and was based on the ligament length and diameter.

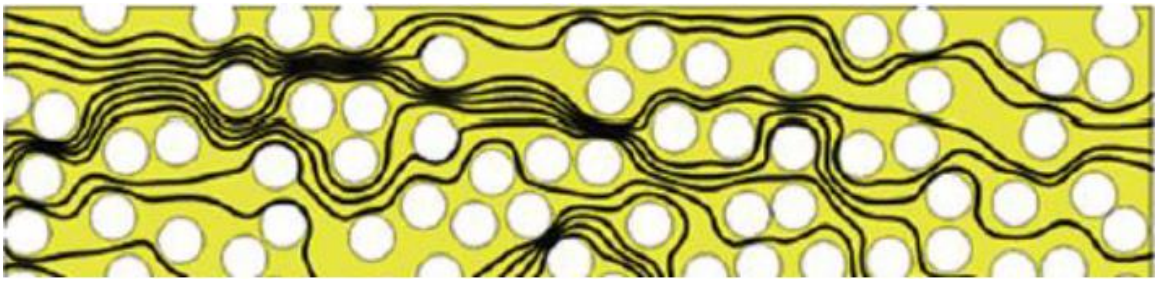

Figure 4.12: Streamlines of flow around cylinders emphasizing tortuosity [55]

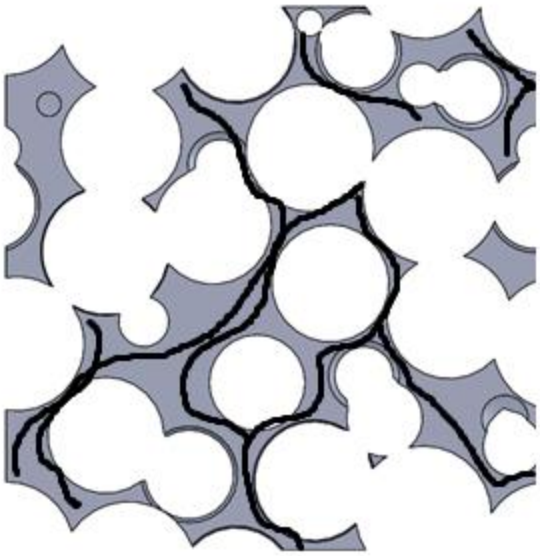

Figure 4.13: Cut section of solid phase structure showing conduction paths. This is analogous to the streamlines shown in Figure 4.12; instead of flow however, heat transfer is represented by the black lines.

There are several types of tortuosity – electric, diffusive, and hydraulic to name a few. These have been studied in numerous papers [55,56]. However, thermal tortuosity is still relatively unstudied. Recall that the effective conductivity of a porous material is made up of the contribution of three terms – the material conductivity, the effects of dispersion, and the effects of tortuosity. Dispersion increases the effective conductivity, while tortuosity has the opposite effect – decreasing the effective conductivity due to the complex conduction path.

The dispersion conductivity in the fluid phase has been studied extensively by DeGroot [48], and the correlation examined in that work was used in the current work. Because the correlation reconciled any major differences in the effective fluid conductivity between the volume averaged level and the pore level, it is assumed that the effects of tortuosity have already been accounted for. It might be relevant to note that in spherical – void phase geometry, the fluid phase is more “spacious” than the solid phase, and especially the fact that the conductivity of the fluid is so much lower than the solid phase. The

combination of these two leads to the fluid tortuosity not affecting the overall heat transfer significantly.

There is no flow in the solid phase, and so no dispersion is added to the conductivity. Recall the equation used to calculate the effective solid conductivity:

$$k_{se} = \frac{k_s}{\tau} * (1 - \varepsilon) + k_{disp} \tag{4.3}$$

In the current code, k_{disp} is 0, but to this point, τ has not been accounted for, meaning the value is left at 1 (which is clearly not the case). As mentioned in the previous section, this assumption is not valid for spherical void-phase geometry, and is the reason for the large discrepancies between the volume-averaged results and the pore level simulations. To find τ, a retroactive approach was taken. Presently, there is no way of calculating the tortuosity factor in the same step as the other parameters: C_f, K, and h_{sf}.

The following procedure is used: preliminary pore-level isothermal simulations are run from which closure parameters are computed; non-isothermal simulations of conjugate heat transfer are also run for comparison with porous continuum results. Once volume-averaged and pore-level results are obtained for a particular geometry, the heat transfer Q is compared. An initial estimate for τ is input into the porous continuum code, and is subsequently adjusted until the heat transfer Q matches the pore level simulations to within a specified tolerance (approximately 5%). The established τ is then the tortuosity factor for that geometric condition. Simulations implementing this factor are examined in subsequent sections, and provide support that the tortuosity has been physically accounted for, and not merely generated by forcing results from different models to match.

Note also that the tortuosity is a function of the geometry, and as such does not depend on the Reynolds number, Prandtl number, or solid phase conductivity. The tortuosity factor was subsequently computed for 6 geometries: porosities 0.75, 0.8, and 0.85 at pore diameters of 400 and 800 microns. The results are summarized in Table 4.4.

Table 4.4: Summary of computed tortuosity factor for different geometries

Porosity	Pore diameter (microns)	Tortuosity τ
0.75	400	2.08
0.8	400	2.22
0.85	400	2.50
0.75	800	2.11
0.8	800	2.23
0.85	800	2.60

4.10 Implementation of tortuosity factor

The tortuosity factor is a function of the solid geometry and conduction path only, and therefore should stay the same no matter the operating conditions. To test this, one case was randomly selected: porosity 0.85, with a pore diameter of 400 microns and water as the working fluid. The conductivity of the porous block was varied from 50,100, 400, and 800 [W/m K]. The range of Reynolds number was from 1 to 200. The same tortuosity factor was used for all simulations. A plot of the bulk heat transfer Q from the various cases is shown in Fig. 4.14. As expected, varying the conductivity while maintaining the tortuosity factor gives very accurate results over the range of conditions studied.

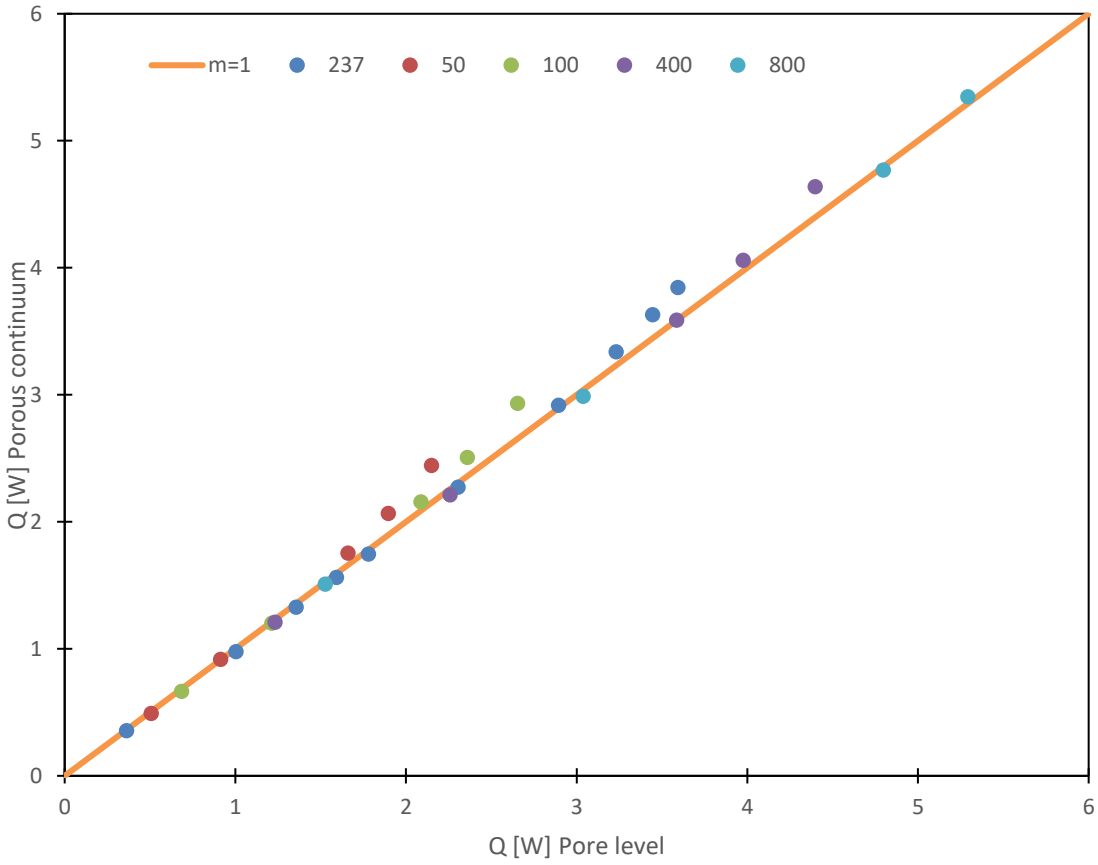

Figure 4.14: Plot showing effects of varying solid phase conductivity on total heat transfer at porosity 0.85, 400 micron diameter and using water.

Figure 4.15 shows a comparison of the total heat transfer Q at porosities 0.75, 0.80, and 0.85 for water at a pore diameter of 400 microns. Also included are the results at porosity 0.75 without the tortuosity factor. This plot shows the significant improvements when the tortuosity in the solid phase conductivity due to the complex conduction path is considered.

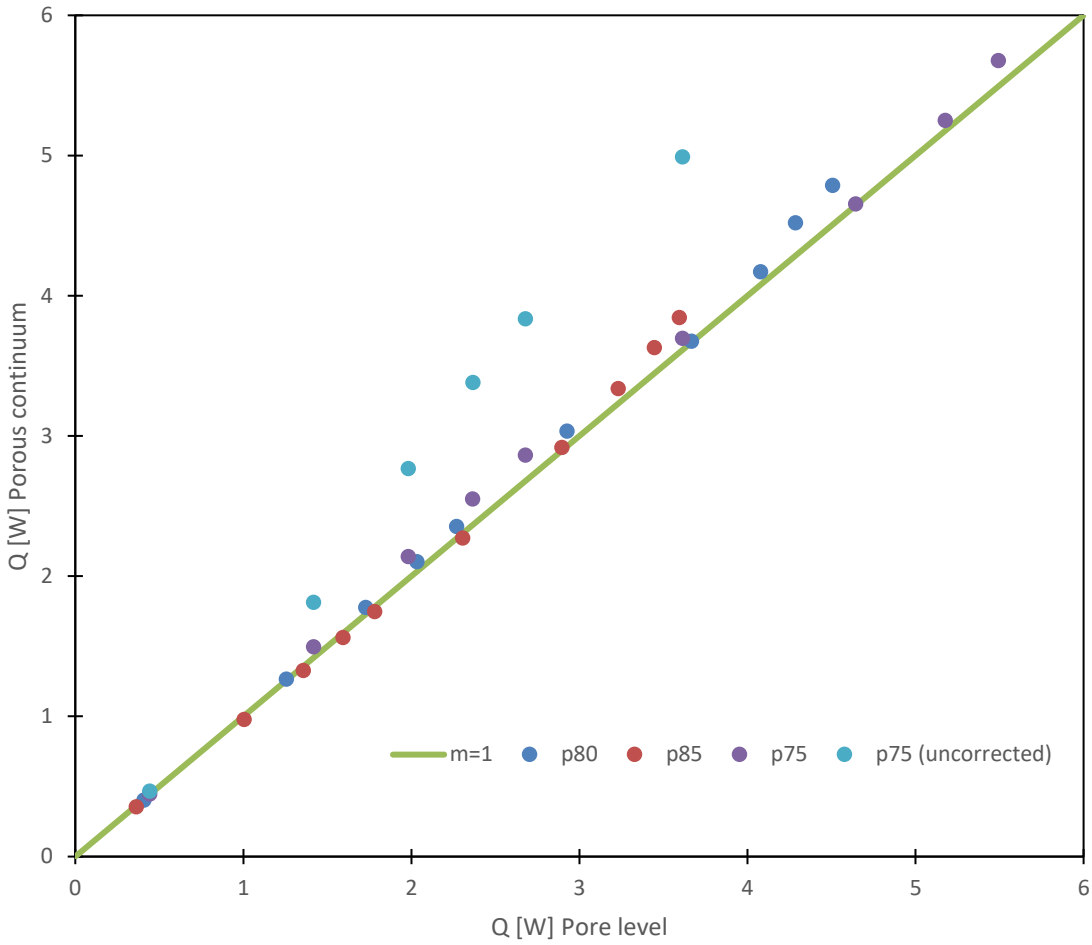

Figure 4.15: Plot showing comparison of total heat transfer calculated using pore level CFD simulations and the porous continuum model (after implementing the tortuosity factor) at different porosities.

When the tortuosity is included, not only is the bulk heat transfer improved, but the temperature profiles are also more accurate. To illustrate this, the average temperature in the vertical direction, at a specified x location, is compared. At a specified X value, a YZ plane is taken. On this plane, several line locations (shown in yellow in Fig. 4.16) are created. At each line, the average temperature along that line is computed. Using this process, the average vertical temperature profile is found. Note that the solid phase and fluid phase temperatures are computed separately. The particular case used is porosity 0.75, 400 micron diameter, and water at Re 20. This is compared with the porous

continuum model, and is shown in Fig. 4.17 and 4.18. A clear improvement can be seen when the tortuosity factor is included.

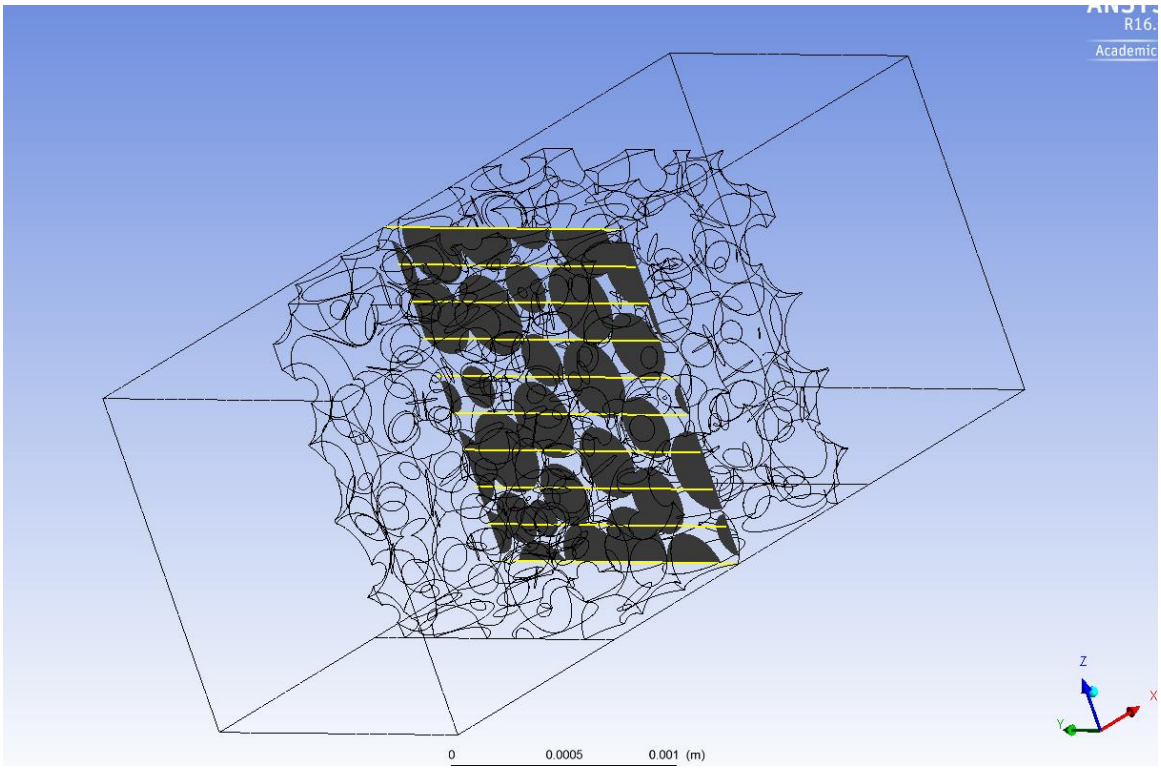

Figure 4.16: Image showing locations of lines along which average temperature is calculated

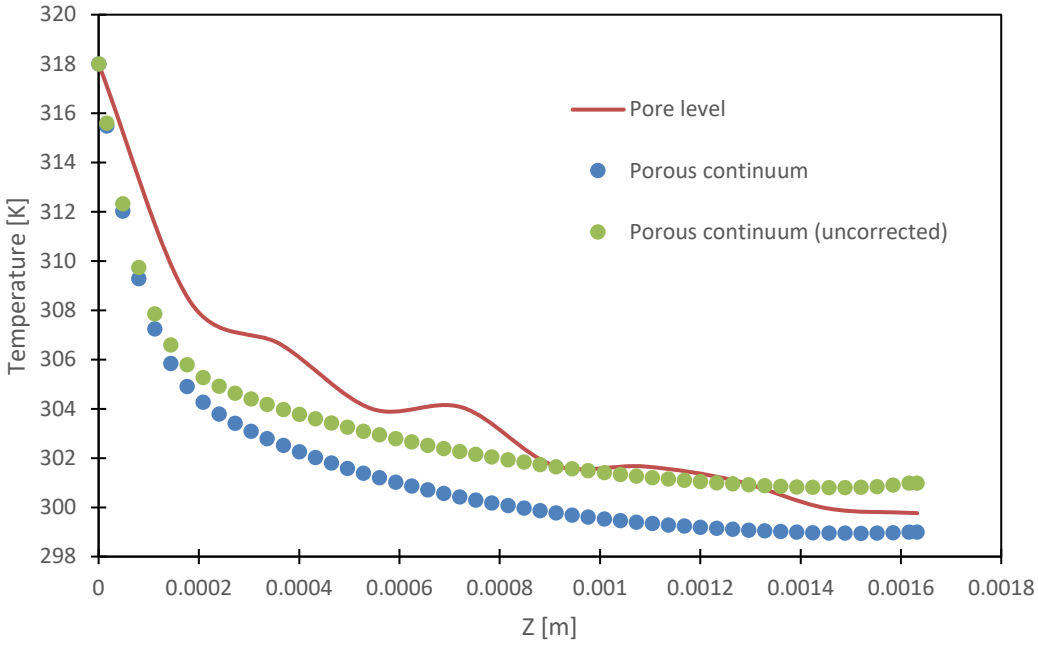

Figure 4.17: Plot showing comparisons between average fluid temperatures along Z axis computed by pore-level simulation and porous continuum model.

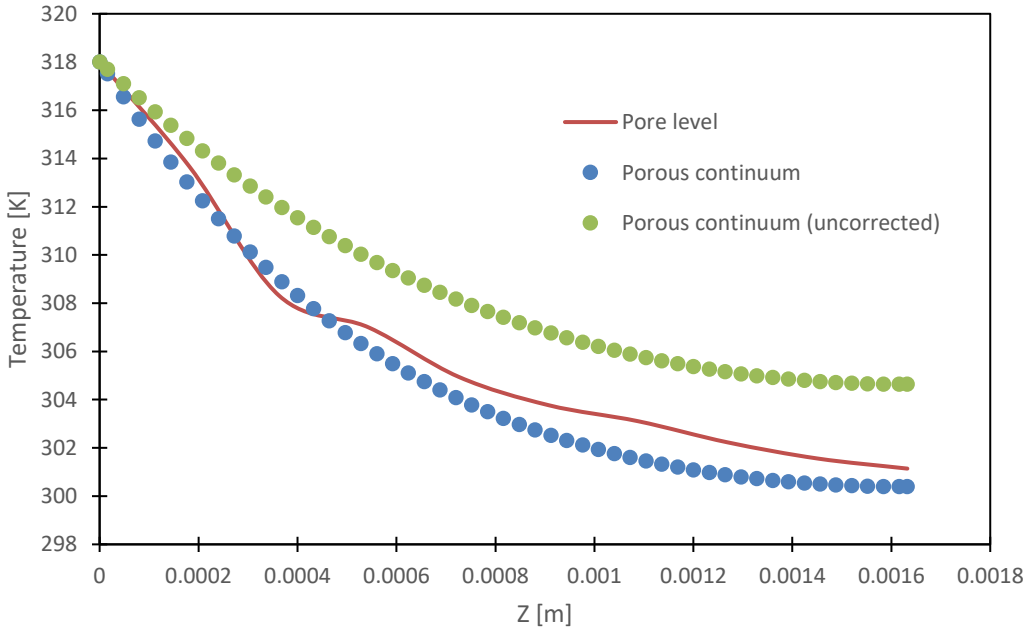

Figure 4.18: Plot showing comparisons between average solid temperatures along Z axis computed by pore-level simulation and porous continuum model.

4.11 Summary

This chapter details the full conjugate simulations performed using both commercial CFD software as well as the porous continuum model. Grid independence was performed, and both set of results were converged to within 5%. It was found that as the Reynolds number increases, the difference between the results generated from the porous continuum model and those generated using CFD software grew, and reached up to 50% at the highest Reynolds number. Two solutions were considered – the first being the addition of a solid substrate at the bottom of the porous block, which would allow the temperature profile to develop more naturally towards the interface between the solid and porous regions. This was found to have no effect, with the errors remaining. The other solution was to modify the calculation of the effective solid phase thermal conductivity. Previously, the tortuosity (which is a measure of how complex a path is) was neglected in the calculation of the conductivity. It was found that this is not an accurate assumption, and the tortuosity must be accounted for. This is due to the conduction path in the solid phase of the porous structure – due to the twisting and winding geometry, as well as the cross-sectional area changes within the solid phase, the effective thermal conductivity is lowered. It was shown that the tortuosity is purely a function of geometry, and does not depend on either the solid phase conductivity or the working fluid.

Chapter 5

5 Summary and Future Work

The objective of this thesis was to investigate and reconcile any significant differences existing between the porous continuum model and pore-level simulations. The porous continuum model solves the volume-averaged momentum and energy equations using a structured, three-dimensional finite-volume CFD code. CFD results of forced convection generated from the porous continuum model and pore-level simulations were compared, and were found to differ significantly. This work determined that there was a missing parameter in the description of the porous material, which was subsequently incorporated into the code, and significantly improved results.

It was found that the closure parameters previously used (the Forcheimer coefficient C_f, the permeability K, and the interstitial heat transfer coefficient h_{sf}) are insufficient when modelling the heat transfer in conjugate simulations involving porous media in which the bottom is heated, and result in large errors, especially when a fluid such as water is chosen.

Two avenues were explored as possible solutions. The first involved adding a solid substrate to the bottom of the porous block, and heating the substrate bottom rather than directly heating the bottom of the porous block, as in previous cases. This allows the temperature profile to develop naturally towards the solid-porous interface, providing a more realistic simulation. Both porous continuum and pore-level simulations were run using this new geometry. It was found that this did not improve the errors, so a second approach was explored. This involved modifying the conductivity of the solid phase in the porous geometry – due to the tortuosity and complexity of the conduction path within the solid matrix, heat transfer resistance is introduced which is captured in the pore-level simulations, but is missing from the porous continuum model. The bulk heat transfer from the porous continuum model now matches much more closely with pore-level simulations, as well as temperature profiles.

5.1 Research conclusions and contributions

Chapter 4 details the conjugate heat transfer cases in which the solid temperature distribution is considered. These were conducted using both pore-level physics (CFD software), and the porous continuum model. The results were compared, and the differences between the two methods indicates a missing element within the porous continuum model. Two possible solutions were investigated – the addition of a solid substrate beneath the porous block, and the modification of the conductivity within the solid phase. The addition of the solid substrate did little to improve the errors.

It was found that a tortuosity factor must be introduced, which accounts or the complex conduction path presented by the geometry of the porous block. By adding in the term, not only did the bulk heat transfer computed by the porous continuum model match much more closely with pore level simulations, but the temperature profiles were improved as well. The tortuosity is purely a function of the geometry of the porous material, as it relates to the conduction path and changing cross sectional areas encountered in the ligaments of the solid phase. The tortuosity is independent of operating conditions such as temperature difference between wall temperature and inlet temperature, material conductivity, and flow field. This was shown through running simulations using the same geometry with varying solid phase conductivities.

5.2 Future work

Currently there is no correlation, or a general equation to find the tortuosity factor. However, it should be noted that if an equation were to be found, at most it would be specific to a particular structures only. Thus, it would also be useful to consider alternate solid structures, such as the reticulated foams measured earlier. The spherical void phase (SVP) geometry was used as it was available, and was shown to be an accurate representation of SVP materials. It would be interesting to compare how the tortuosity differs between geometries.

Because of time constraints, only six cases were considered in this thesis (two pore diameters, at three porosities each). Future work could focus on collecting more data

from cases, and seeing whether a trend or pattern exits. As of now, it is still unclear what geometric property correlates the most to tortuosity. Another future project could look at a new method of determining the tortuosity factor directly from the pore level simulations without having to resort to the retroactive comparison shown in the present work, which is a tedious process. Tying in with the previous suggestion, a correlation relating geometric properties such as pore diameter, porosity, surface area to volume ratio, or ligament length, or any combination of these, would be extremely helpful. Again, more data would have to be collected before any significant conclusion can be made.

6 References

[1] Calmidi, V. V. and Mahajan, R. L., 2000, "Forced convection in high porosity metal foams," J. Heat Transfer, **122**(3), pp. 557–565

[2] Yu, Q., Straatman, A. G., and Thompson, B. E., 2006, "Carbon-foam finned tubes in air-water heat exchangers," Applied Thermal Engineering, 26, pp. 131–143.

[3] Straatman, A. G., Gallego, N. C., Thompson, B. E., and Hangan, H., 2006, "Thermal characterization of porous carbon foam – convection in parallel flow," Int. J. Heat Mass Transfer, 49, pp. 1991–1998.

[4] Straatman, A. G., Gallego, N. C., Yu, Q., and Thompson, B. E., 2007, "Characterization of porous carbon foam as a material for compact recuperators," J. Engineering Gas Turbines and Power, 129(2), pp. –1245.

[5] Straatman, A. G., Gallego, N. C., Yu, Q., Betchen, L. J., and Thompson, B. E., 2007, "Forced convection heat transfer and hydraulic losses in graphitic foam," J. Heat Transfer, 129, pp. 1237–1245.

[6] Sultan, K., DeGroot, C. T., Straatman, A. G., Gallego, N. C., and Hangan, H., 2009, "Thermal characterization of porous graphitic foam – convection in impinging flow," Int. J. Heat Mass Transfer, **52**(19-20), pp. 4296-4301

[7] Betchen, L., 2005, "A Non-Equilibrium Finite-Volume Model for Conjugate Fluid/Porous/Solid Domains," MESc. Thesis, Western University, London, Ontario, Canada

[8] Bhattacharya, A., Calmidi, V. V., and Mahajan, R. L., 2002, "Thermophysical properties of high porosity metal foams," Int. J. Heat Mass Transfer, 45(5), pp. 1017–1031.

[9] Whitaker, S., 1996, "The Forchheimer equation: A theoretical development," Transport in Porous Media, **25**, pp. 27–61.

[10] Quintard, M., Kaviany, M., and Whitaker, S., 1997, "Two-medium treatment of heat transfer in porous media: Numerical results for effective properties," Adv. Water Resources, **20**(2), pp. 77–94.

[11] Sahraoui, M. and Kaviany, M., 1994, "Slip and no-slip temperature boundary conditions at the interface of porous, plain media: Convection," Int. J. Heat Mass Transfer, **37**(6), pp. 1029–1044.

[12] Kuwahara, F., Nakayama, A., and Koyama, H., 1996, "A numerical study of thermal dispersion in porous media," J. Heat Transfer, **118**, pp. 756–761.

[13] Souto, H. P. A. and Moyne, C., 1997, "Dispersion in two-dimensional periodic porous media. Part II. Dispersion tensor," Phys. Fluids, **9**(8), pp. 2253–2263.

[14] Kuwahara, F. and Nakayama, A., 1999, “Numerical determination of thermal dispersion coefficients using a periodic porous structure,” J. Heat Transfer, **121**(1), pp. 160–163.

[15] Kuwahara, F., Shirota,M., and Nakayama, A., 2001, “A numerical study of interfacial convective heat transfer coefficient in two-energy equation model for convection in porous media,” J. Heat Transfer, **118**, pp. 756–761.

[16] Kaviany, M., 1995, *Principles of Heat Transfer in Porous Media*, Springer-Verlag, New York, NY, 2nd ed.

[17] Ward, J. C. 1964, “Turbulent Flow in porous media,” Proceedings of the American Society of Civil Engineers, **90**(HY5), pp. 1-12

[18] Callego, N. C. and Klett, J. W., 2003, “Carbon foams for thermal management,” Carbon, **41**(7), pp. 1461-1466

[19] Straatman, A. G., Gallego, N. C., Yu, Q., Betchen, L. and Thompson, B. E., 2006, “Forced convection heat transfer and hydraulic losses in graphitic foam,” J. Heat Transfer, **129**(9), pp. 1237-1245

[20] Fu, X., Viskanta, R. and Gore, J.P., 1998, “Measurement and correlation of volumetric heat transfer coefficients of cellular ceramics,” Exp. Thermal and Fluid Science, **17**(4), pp. 285-293

[21] Kamiuto, K. and Yee, S. S., 2005, “Heat transfer correlations for open cellular porous materials,” Int. Commun. Heat Mass Transf., **32**, pp. 947-953

[22] Younis L. B,. and Viskanta, R., 1993, “Experimental determination of the volumetric heat transfer coefficient between stream of air and ceramic foam,” Int. J. Heat Mass Transf., **36**, pp. 1425-1434

[23] Ichimiya, K., 1999, “A new method for evaluation of heat transfer between solid material and fluid in a porous medium,” ASME J. Heat Transf., **121**, pp. 978–983

[24] Ando, K., Hirai, H., Sano, Y., 2014 “An Accurate Experimental Determination of Interstitial Heat Transfer Coefficients of Ceramic Foams Using the Single Blow Method,” The Open Transport Phenomena Journal, **5**, pp. 7-12

[25] Jambhekar, V.A., 2011,” Forchheimer Porous-media Flow Models - Numerical Investigation and Comparison with Experimental Data,” Ph.D. thesis, Lehrstuhl für Hydromechanik und Hydrosystemmodellierung, Universität Stuttgart, Stuttgart, Germany

[26] Calmidi, V.V., 2000, “Forced Convection in High Porosity Metal Foams,” J. Heat Transfer, **122**(3), pp. 557-565

[27] Haussener, S., Coray, P., Lipinski W., Wyss, P. and Steinfeld, A., 2010, "Tomography-based heat and mass transfer characterization of reticulate porous ceramics for high-temperature processing," J. Heat Transfer, **132**(2), pp. 023305

[28] Haussener, S., Jerjen, I., Steinfeld, A., and Wyss, P., 2011 "Tomography-based determination of effective transport properties for reacting porous media.," Journal of Heat Transfer, **134**(1), pp. 012601-012601

[29] Haussener, S., Lipinski, W., Wyss, P. and Steinfeld, A., 2010, "Tomography-based analysis of radiative transfer in reacting packed beds undergoing a solid-gas thermochemical transformation," J. Heat Transfer **132**(6), pp. 061201

[30] Zermatten, E., Haussener, S., Schneebeli, M. and Steinfeld, A., 2011, "Tomography-based determination of permeability and Dupuit–Forchheimer coefficient of characteristic snow samples," J. Glaciol. **57**(205), pp. 811-816

[31] Yu, Q., Thompson, B.E. and Straatman, A. G., 2006, "A unit cube-based model for heat transfer and fluid flow in porous carbon foam," Journal of Heat Transfer, **128**(4), pp. 352- 360

[32] Boomsma, K., and Poulikakos, D., 2001, "On the effective thermal conductivity of a three dimensionally structured fluid-saturated metal foam," Int. J. Heat Mass Transfer **44**(4), pp. 827-836

[33] Kumar, P., Hugo, J., Topin, F. and Vicente. J., 2012, "Influence of pore and strut shape on open cell metal foam bulk properties," AIP Conference Proceedings, **1453**(1), pp. 243-248

[34] Leong, K. C. and Li, H. Y., 2011, "Theoretical study of the effective thermal conductivity of graphite foam based on a unit cell model," Int. J. Heat Mass Transfer, **54**(25–26), pp. 5491-5496

[35] Kırca, M., Gül, A., Ekinci, E., Yardım, F. and Mugan, A., 2007, "Computational modeling of micro-cellular carbon foams," Finite Elements Anal. Des., **44**(1–2), pp. 45-52

[36] Wang, M. and Pan, N., 2008, "Modeling and prediction of the effective thermal conductivity of random open-cell porous foams," Int. J. Heat Mass Transfer, **51**(5–6), pp. 1325-1331

[37] Chueh, C. C., Bertei, A., Pharoah, J. G. and Nicolella, C., 2014, "Effective conductivity in random porous media with convex and non-convex porosity," Int. J. Heat Mass Transfer, **71**(0), pp. 183-188

[38] Dyck, N., 2014 "Digital Generation and Radiation in Spherical Void-Phase Porous Media," MESc. Thesis, Western University, London, Ontario, Canada

[39] Kopanidis, A., Theodorakakos, A., Gavaises, E. and Bouris, D., 2010, "3D numerical simulation of flow and conjugate heat transfer through a pore scale model of high porosity open cell metal foam," Int. J. Heat Mass Tran. **53**(11–12), pp. 2539–2550.

[40] Bianchi, E., Groppi, G., Schwieger, W., Tronconi, E. and Freund, H., 2015, "Numerical simulation of heat transfer in the near-wall region of tubular reactors packed with metal open-cell foams," Chem. Eng. J., **264**, pp. 268–279

[41] Petrasch, J., Meier, F., Friess, H. and Steinfeld, A., 2008, "Tomography based determination of permeability, Dupuit-Forchheimer coefficient, and interfacial heat transfer coefficient in reticulate porous ceramics," Int. J. Heat Fluid Flow, **29**(1), pp. 315–326.

[42] Della Torre, A., Montenegro, G., Tabor, G.R. and Wears, M.L., 2014, "CFD characterization of flow regimes inside open cell foam substrates," Int. J. Heat Fluid Flow, **50**, pp. 72–82.

[43] Meinicke, S., Wetzel, T. and Dietrich, B., 2017, "Scale-resolved CFD modelling of single-phase hydrodynamics and conjugate heat transfer in solid sponges," Int. J. Heat and Mass Transf., **108**, pp. 1207-1218

[44] Bodla, K.K., Murthy, J.Y. and Garimella, S.V., (2010) "Resistance network-based thermal conductivity model for metal foams", Computational Materials Science, **50**, pp. 622-632

[45] Karimian, S. A. M. and Straatman, A. G., 2009, "Numerical modeling of multidirectional flow and heat transfer in graphitic foams," J. Heat Transfer, **131**, pp. 052602–1–11

[46] Straatman, A. G., Kalopsis, A., and Dyck, N., 2016, "Generation of simple extended porous surface expression from results of pore-level conjugate heat transfer in spherical-void-phase porous blocks," Sixth International Conference on Porous Media and Its Applications in Science, Engineering and Industry, Eds, ECI Symposium Series

[47] Beavers, G. and Joseph, D.D., 1967, "Boundary Conditions at a Naturally Permeable Wall," J. Fluid Mech., **30**, pp.197-207

[48] DeGroot, C., 2009, "Numerical Modeling of Thermal Dispersion and Viscous Effects in High-Conductivity Porous Materials," MESc. Thesis, Western University, London, Ontario, Canada

[49] Zhang, L., 2014, "Comparison of volume-average simulation and pore-scale simulation of thermal radiation and natural convection in high temperature packed beds" 5th International Conference on Porous Media and their Applications in Science, Engineering, and Industry

[50] Costa, V.A.F., Oliveira, L. A. and Baliga, B.R., 2008, "Implementation of the Stress Jump Condition in a Control-Volume Finite-Element Method for the Simulation of

Laminar Coupled Flows in Adjacent Open and Porous Domains," Num. Heat Transf. Part B: Fundamentals, **53**(5), pp. 383-411

[51] DeGroot, C.T., Straatman, A.G. and Betchen, L.J., 2009, "Modeling forced convection in finned metal foam heat sinks," ASME J. Electron. Pack., **131**(2), pp. 021001–021010

[52] "Steady-state Time Scale Control" Retrieved from: https://www.sharcnet.ca/Software/Ansys/16.2.3/en-us/help/cfx_mod/i1313401.html

[53] Klett, J., McMillan, A., Gallego, N. and Walls, C., 2004, "The role of structure on the thermal properties of graphitic foams," J. Mater. Sci., **39**(11), pp. 3659–3676.

[54] Ouyang, X. L., Jiang, P.X. and Xu, R. N., 2013 "Thermal boundary conditions of local thermal non-equilibrium model for convection heat transfer in porous media," Int. J. Heat Mass Transf., **60**, pp. 31-40

[55] Saomoto, H. and Katagiri, J., 2015, "Direct comparison of hydraulic tortuosity and electric tortuosity based on finite element analysis," Theor. Appl. Mech. Lett., **5**(5), pp. 177-180

[56] Boudreau, B. P., 1996, "The diffusive tortuosity of fine-grained unlithified sediments," Geochimica et Cosmochimica Acta, **60**(16), pp. 3139-3142

Curriculum Vitae

Name:	Jeremy Vu
Post-secondary Education and Degrees:	British Columbia Institute of Technology Burnaby, British Columbia, Canada 2011-2015 B.Eng.
Honours and Awards:	Robert B. Wells and Family Award Scholarship 2014
Related Work Experience	Teaching Assistant The University of Western Ontario 2015-2016